Gelatin/PEDOT: PSS Modified Manganese Dioxide Cathode in Aqueous Rechargeable Zinc-ion Batteries

by

Qiuyu Shi

A thesis
presented to the University of Waterloo
in fulfillment of the
thesis requirement for the degree of
Master of Applied Science
in
Chemical Engineering (Nanotechnology)

Waterloo, Ontario, Canada, 2021

AUTHOR'S DECLARATION

I hereby declare that I am the sole author of this thesis. This is a true copy of the thesis, including any required final revisions, as accepted by my examiners.

I understand that my thesis may be made electronically available to the public.

Abstract

The global energy crisis and greenhouse effect have become important problems in the 21st century, and researchers have paid attention to renewable energy, including hydro, wind, solar and nuclear energy sources. However, some of them are not always available. Energy storage systems become critical for their availability, and batteries are most commonly used to this end. Although lithium-ion batteries take up most of the portable battery market, it still has safety, cost, and environmental concerns. A battery with high energy density, high safety, cost efficiency, and environmental friendliness is strongly in demand. The aqueous rechargeable Zn-MnO_2 battery has attracted many researchers' attention due to its high energy density, high safety, low cost, and low toxicity. However, the cycling performance of this battery is not very satisfactory because of the Mn dissolution problem. Therefore, two effective strategies were proposed and conducted in this project to overcome the Mn dissolution issue and improve the electrochemical performance of the battery.

First, the ε-MnO_2 material was synthesized by an innovative, safe, and cost-effective co-precipitation method. Compared to the commercial MnO_2 material with poor electrochemical performance and the MnO_2 material synthesized by dangerous hygrothermal methods in labs, this new co-precipitation method is simple, safe, and cheap. More importantly, the ε-MnO_2 material exhibits an excellent specific discharging capacity of 330 mAh/g at 50 mA/g when applied in the aqueous rechargeable Zn-MnO_2 battery.

However, the cyclability of the battery is not outstanding with only 20 cycles at 50 mA/g and 200 cycles at 500 mA/g at 80% capacity retention.

To improve the battery's cycling performance, gelatin was coated on top of the ε-MnO_2 cathode by spin coating. Gelatin can confine Mn^{2+} near the cathode through hydrogen bonding and van der Waal's force, thereby effectively controlling the Mn dissolution and improving the battery cyclability to 1000 cycles with 80% capacity retention at 500 mA/g, which is a remarkable improvement in the cycling performance of the aqueous rechargeable Zn-MnO_2 battery.

Another strategy was conducted to improve the battery cyclability. Since PEDOT: PSS is a highly conductive polymer with negatively charged deprotonated sulfonyl group, it could attract Mn^{2+} through ionic interactions, which can regulate the Mn dissolution problem. Benefiting from the PEDOT: PSS coating on ε-MnO_2 cathode, the battery showed a good cycling peroformance of 250 cycles at 500 mA/g and 50 cycles at 50 mA/g with both 80% capacity retention.

These strategies have increased the cyclability of the aqueous rechargeable Zn-MnO_2 battery up to 1000 cycles with 80% capacity retention, which is a dramatic enhancement of the cycling performance. They not only opened new ways for other researchers to further develop the battery performance, but also accelerate the application progress of aqueous rechargeable Zn-MnO_2 batteries.

Acknowledgements

The work herein was financially supported by Mitacs through the Mitacs Accelerate program and the University of Waterloo.

First, I would like to express my great gratitude to my supervisor, Professor Pu Chen, for providing me this great opportunity to pursue my graduate studies and for his continuous and valuable guidance and support throughout the master's program.

I would like to acknowledge my advisory committee members, Professor Eric Croiset and Professor Yuning Li, for their time and constructive feedback towards the completion of this thesis.

I would like to thank my former and current colleagues including Dr. Yu Liu, Dr. Joseph Palathinkal Thomas, Dr. Mina Sedighi, Mei Han, Yan Wu, Zhongyi Liu, Yuxiao Jiao, and Feng Zhao for their continuous assistance and support.

Last but not least, I am really grateful to my grandparents, Xiushan Zhang and Jinzhi Pei, my parents, Yong Shi and Yuhong Zhang, and my boyfriend, Chenwei Zhang, for their endless love, support, and encouragement during my master's study.

Table of Contents

AUTHOR'S DECLARATION ii
Abstract iii
Acknowledgements v
List of Figures viii
List of Tables viii
Chapter 1 : Introduction 1
1.1 Introduction 1
1.2 Aqueous Rechargeable Zinc Ion Batteries (ARZBs) 9
1.3 Cathode materials for ARZBs 11
1.4 Zn-MnO_2 system 15
1.4.1 Storage mechanism of aqueous rechargeable Zn-MnO_2 battery system 16
1.4.2 Advantages and limitations of aqueous rechargeable Zn-MnO_2 battery system 18
1.4.3 Strategies to overcome limitations of aqueous rechargeable Zn-MnO_2 battery system 20
1.5 Gelatin 23
1.5.1 Properties 26
1.5.2 Applications 27
1.6 PEDOT: PSS polymer 29
1.6.1 Properties 29
1.6.2 Applications 30
1.7 Project Scope and Objectives 33
Chapter 2 : Characterization Techniques 34
2.1 Material Characterization Techniques 34
2.1.1 Scanning Electron Microscope (SEM) 34
2.1.2 X-ray Diffraction (XRD) 36
2.1.3 Fourier Transform Infrared Spectroscopy (FTIR) 39
2.1.4 X-Ray Photoelectron Spectroscopy (XPS) 40

2.2 Electrochemical Characterization Techniques 42
2.2.1 Cyclic Voltammetry (CV) 42
2.2.2 Battery Capacity Test 44
2.2.3 Battery Cyclability Test 45
2.2.4 Battery Rate Capability Test 46
Chapter 3 : Gelatin coated self-made ε-MnO_2 as cathode material in aqueous rechargeable zinc-ion batteries 47
3.1 Synthesis of self-made ε-MnO_2 and preparation of gelatin solutions 47
3.1.1 Synthesis of self-made ε-MnO_2 47
3.1.2 Prepare gelatin solutions 48
3.2 Cathode Fabrication and Battery Assembling 49
3.3 Material Characterizations 52
3.4 Electrochemical Characterizations 57
3.5 Conclusions 64
Chapter 4 : PEDOT: PSS coated self-made ε-MnO_2 as cathode material in aqueous rechargeable zinc-ion batteries 66
4.1 Preparation of PEDOT: PSS solutions 66
4.2 Cathode Fabrication and Battery Assembling 67
4.3 Material Characterizations 67
4.4 Electrochemical Characterizations 70
4.5 Conclusions 74
Chapter 5 : Summary of the Thesis 77
References 79

List of Figures

Figure 1 Electricity generation mix in advanced economies, 1971-2019[2] 2
Figure 2 Worldwide battery market 1990-2018[6] 4
Figure 3 Lead-acid battery chemistry: (a) during discharging, (b) during charging, and (c) battery prototype[9] 5
Figure 4 Nickel-based battery chemistry: (a) during discharging, (b) during charging, and (c) battery prototype[9] 7
Figure 5 Lithium-ion battery chemistry: (a) during discharging and charging, and (b) cylindrical view of LIB[9] 8
Figure 6 A Schematic of the chemistry inside ARZBs[25] 10
Figure 7 a) Ragone plot of typical representative cathode materials for AZIBs. b) Comparison of the main cathode families in benefits (black) and limitations (red)[28] 12
Figure 8 Crystal structures of α-, β-, γ-, λ-, and δ-MnO_2[28] 16
Figure 9 Schematics and energy storage mechanisms of Zn/MnO_2 battery[35] 17
Figure 10 The formation and growth mechanism of zinc dendrites in ARZBs[45] 20
Figure 11 Challenges and optimization strategies in aqueous ZIBs system[41] 22
Figure 12 Hydrolysis process of collagen to produce gelatin[53] 24
Figure 13 Basic chemical structure of gelatin[54] 25
Figure 14 Amino acid composition of gelatin[54] 25
Figure 15 A schematic of the gelatin electrode microskin in aqueous rechargeable Zn-MnO_2 battery system[31] 28
Figure 16 The chemical structure of the PEDOT: PSS[70] 29
Figure 17 (a) A schematic of the flexible solid-state electrolyte Zn-MnO_2@PEDOT battery; (b) SEM image the Zn anode; (d) SEM images and (e) HRTEM images of the MnO_2@PEDOT sample[75] 32
Figure 18 A schematic of the scanning electron microscopy with main components[77] . 35
Figure 19 A schematic of the X-ray diffraction equipment[79] 37
Figure 20 Illustration of the Bragg's diffraction[80] 38

Figure 21 A schematic of an interferometer in a Fourier transform infrared spectrometer[84] 40
Figure 22 (a) A schematic of X-ray photoelectron spectrometer; (b) The diagram of XPS working principle[86,87] 41
Figure 23 The cyclic voltammetry potential waveform[90] 43
Figure 24 A typical cyclic voltammogram[91] 44
Figure 25 An image of the NEWARE BTS4000-5V battery tester[92] 45
Figure 26 A schematic of main procedures to synthesize **ε**-MnO_2 48
Figure 27 A picture of 0.3 wt%, 0.5 wt%, 0.7 wt%, 1 wt%, 3 wt% and 5 wt% gelatin solutions 49
Figure 28 The basic structure of the aqueous rechargeable Zn-MnO_2 battery[94] 50
Figure 29 Hydraulic crimping machine (MTI, MSK-100)[95] 51
Figure 30 Chemat precision spin-coater (Sigma-Aldrich, Z551562)[96] 52
Figure 31 SEM images of ε-MnO_2 in different scales 53
Figure 32 A SEM image of 0.5 wt% gelatin coated ε-MnO_2 53
Figure 33 XRD result of self-made MnO_2 powder 54
Figure 34 FTIR results of MnO_2 and gelatin coated MnO_2 cathode 55
Figure 35 XPS spectra of (a) survey spectrum and (b) Mn 2p spectrum of MnO_2 cathode; (c) survey spectrum and (d) N 1s spectrum of 0.5 wt% gelatin coated MnO_2 cathode 57
Figure 36 The cyclic voltammograms of (a) 1st cycle and (b) 1-3 cycles of Zn-MnO_2 battery with unmodified cathode, and (c) 1st cycle and (d) 1-3 cycles of Zn-MnO_2 battery with 0.5 wt% gelatin coated cathode 59
Figure 37 The battery capacity tests for an unmodified Zn-MnO_2 battery (left) and a Zn-MnO_2 battery with gelatin coated cathode (right) 60
Figure 38 The battery cycling performance of unmodified Zn-MnO_2 battery at (a) 50 mA/g and (b) 500 mA/g, and the cycling performance of gelatin coated Zn-MnO_2 battery at (c) 50 mA/g and (d) 500 mA/g 62

Figure 39 The rate performance of the unmodified Zn-MnO_2 battery (left) and the gelatin coated Zn-MnO_2 battery (right) at 0.05 A/g, 0.1 A/g, 0.2 A/g, 0.5 A/g, 1 A/g and 2 A/g..... 64
Figure 40 A picture of the prepared EM-10, EM-16 and EM-20 solutions..... 66
Figure 41 A SEM image of the PEDOT: PSS coated MnO_2 cathode..... 67
Figure 42 FTIR results of PEDOT: PSS coated MnO_2 cathode..... 68
Figure 43 XPS spectra of the survey spectrum (left) and S 2p spectrum (right) of the PEDOT: PSS coated MnO_2 cathode..... 69
Figure 44 The cyclic voltammograms of 1st cycle (left) and 1-3 cycles (right) of Zn-MnO_2 battery with PEDOT: PSS coated MnO_2 cathode..... 71
Figure 45 The battery capacity tests of a Zn-MnO_2 battery with PEDOT: PSS coated MnO_2 cathode..... 72
Figure 46 The battery cycling performance of the PEDOT: PSS coated Zn-MnO_2 battery at 50 mA/g (left) and 500 mA/g (right)..... 73
Figure 47 The rate performance of the PEDOT: PSS coated Zn-MnO_2 battery at 0.05 A/g, 0.1 A/g, 0.2 A/g, 0.5 A/g, 1 A/g and 2 A/g..... 74

List of Tables

Table 1 Summary of electrochemical performances of various cathode materials for aqueous zinc-ion batteries[24] 14

Chapter 1: Introduction

1.1 Introduction

The energy crisis has become one of the most important, necessary and urgent problems for humanity in the 21st century, and people have paid more and more attention on the renewable energy now.[1] As shown in Figure 1, it is a report from the International Energy Agency about electricity generation mix in advanced economies from 1971-2019.[2] The usage precents of three main non-renewable energy: coal, oil, and gas has relatively decreased from 1970-2019 while the usages percent of renewable energy has increased. Nowadays, the most widely used renewable energy are hydro energy, wind energy, solar energy, and nuclear energy. However, some of them may not be always available and stable. For example, the electricity produced from wind and solar energy depends on the weather, and the hydro energy depends on the season and weather. Therefore, in order to obtain stable and continuous electricity generated by renewable energy, energy storage systems have become the key part of the whole process. With a stable electricity supplier, people could use it anytime and anywhere without being restricted by nature or weather.

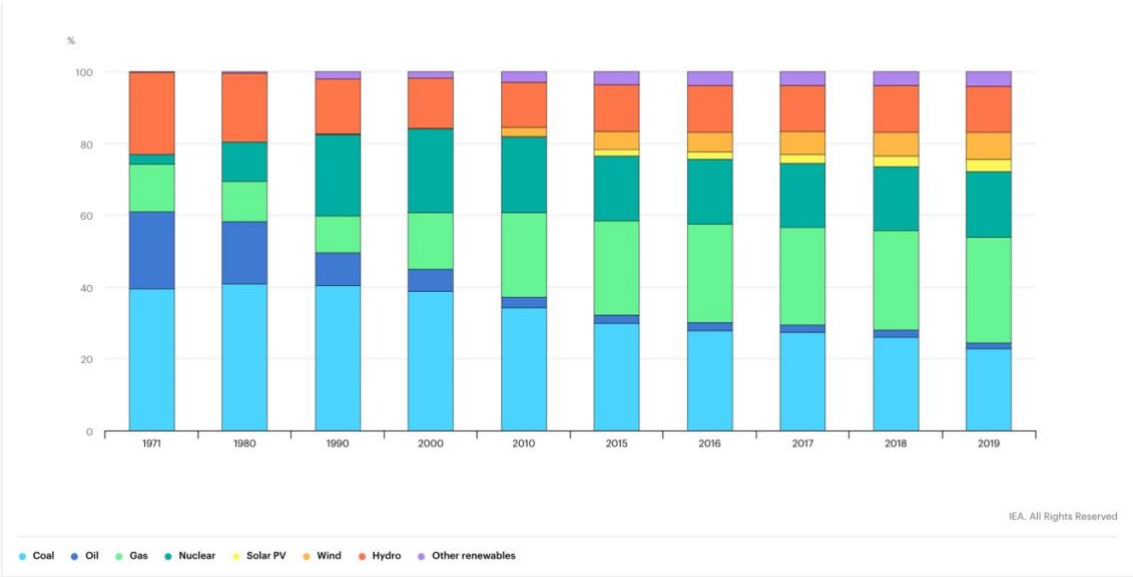

Figure 1 Electricity generation mix in advanced economies, 1971-2019[2]

The emerging energy storage systems include batteries, fuel cells, supercapacitors, pumped hydro storage and thermal energy storages, etc.[3] Among these energy storage systems, batteries are the most commonly used ones in the daily life, and they could be found in cellphones, laptops, electric vehicles and even power stations. Therefore, conducting research in the field of batteries could be very critical and beneficial for humanity.

A battery is a device that can convert chemical energy directly into electricity by redox reactions, and it is consisting of three main components: cathode, anode and electrolyte.[4] The reduction reaction occurs at cathode and it receives electrons while the oxidation reaction takes place at anode and it donates electrons. The electrolyte is the ionic conductor, and it provides the medium for charge transfer between the cathode and anode.[4]

Batteries can be classified into primary batteries and secondary batteries.[5] The primary batteries couldn't be recharged once depleted, and commonly used primary batteries are Leclanché batteries, alkaline batteries and zinc air batteries, etc.[4] They are simple, cheap and convenient, and have a wide variety of applications, but could not be recharged. Moreover, the recycle and pollution problems also limit their further development. Afterwards, another type of batteries become popular because of their rechargeability, and these are secondary batteries. Lead-acid batteries, nickel cadmium batteries (NiCD), nickel-metal hydride batteries (NiMH), and lithium-ion batteries (LIB) are all widely used secondary batteries in the market. They could act as energy storage systems and have wide applications in electronic devices and even electric vehicles.

As shown in Figure 2, it is a report of the worldwide battery market from 1990 to 2018.[6] The figure shows an increasing demand of the whole battery market since 1990. More specifically, lead-acid batteries are the most widely used rechargeable batteries to date around the world, and lithium-ion batteries market is increasing rapidly. The nickel cadmium and nickel-metal hydride batteries demand does not have significantly change these years compared to other batteries. Other new types of batteries also appear in the market, such as flow batteries and sodium–sulfur batteries (NAS). These batteries have played important roles in the market, and they are changing people's lifestyle as well. However, they both have advantages and limitations.

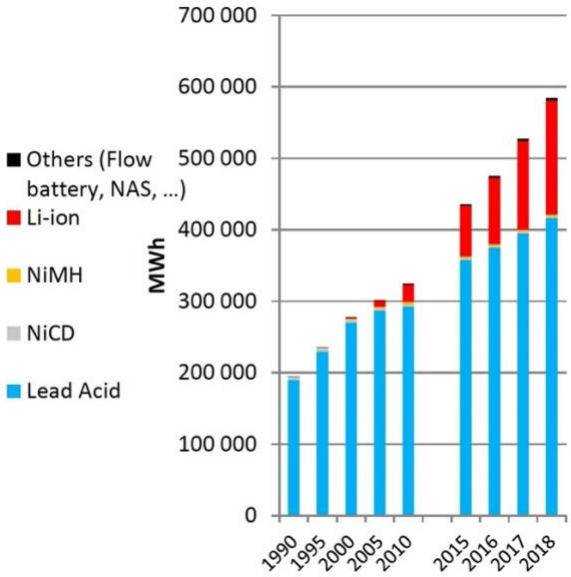

Figure 2 Worldwide battery market 1990-2018[6]

Lead-acid battery was first invented by Gaston Planté in 1859.[7] 150 years development let it become the most widely used rechargeable battery in the world.[8] The cathode material is lead dioxide (PbO_2) while the anode material is lead (Pb), and the electrolyte is diluted sulfuric acid (H_2SO_4). During the discharge process, the cathode and anode will both react to form lead sulfite ($PbSO_4$). Moreover, the battery chemistry during the whole discharging and charging process are also shown in Figure 3. The overall discharge reaction is shown below.

$$PbO_2 + Pb + 2H_2SO_4 \rightleftharpoons 2PbSO_4 + 2H_2O$$

Lead-acid battery has proven to be low-cost, recyclable, easy to manufacture and good high-rate performance.[8] It has a wide application in automobiles, electric vehicles, energy storage system, uninterrupted power supply systems, and industry.[4] However, it has a low energy density and relatively low cycle life. Long-term storage in a discharged state leads

to sulfation of the battery, causing irreversible damage.[8] These problems limit its further development in portable devices applications.

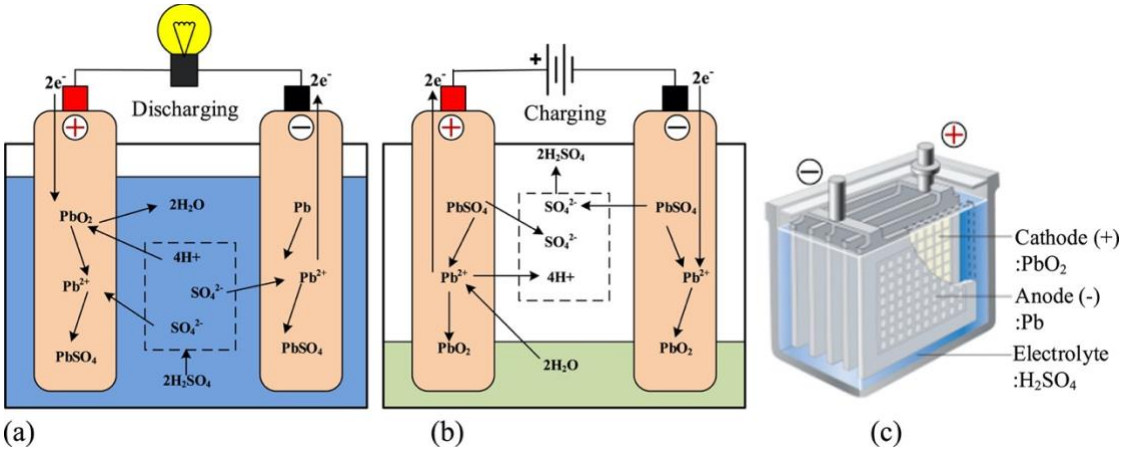

Figure 3 Lead-acid battery chemistry: (a) during discharging, (b) during charging, and (c) battery prototype[9]

Nickel cadmium battery was invented by Waldemar Jungner in 1899.[4] It is one of the most common rechargeable batteries, and it has been classified into small consumer cells and large industrial batteries.[10] The cathode material is nickel oxide hydroxide (NiOOH), the anode material is cadmium (Cd), and the electrolyte is usually an alkaline electrolyte (such as potassium hydroxide, KOH). The overall discharge reaction is listed below.

$$2NiOOH + Cd + 2H_2O \rightleftharpoons 2Ni(OH)_2 + Cd(OH)_2$$

Nickel cadmium battery has various applications in cordless electric utensils, cordless telephones, airplane engine starters, and communicational distribution systems.[10] It has a long cycle life, rapid recharge capability, good low-temperature and high-rate performance capability, and safety vent system.[4] However, it also has some limitations. It has a higher cost, poor charge retention, and lower capacity than other competitive batteries.[4] Moreover,

due to the use of cadmium, it can pollute the environment and may have serious effect on human health.[11] Therefore, these limitations dramatically weaken its application and competitivity.

Nickel-metal hydride battery has been widely used since its invention in the 1970s.[12] During the discharge process, the cathode material metal hydride (MH) will be oxidized to the metal alloy, and the anode material nickel oxyhydroxide (NiOOH) will be reduced to nickel hydroxide ($Ni(OH)_2$). The battery chemistry and prototype are also shown in Figure 4 below. The overall discharge reaction is shown below as well.[4]

$$NiOOH + MH \rightleftharpoons Ni(OH)_2 + M$$

Nickel-metal hydride battery exhibits many advantages, including high energy and power density, high current charge and discharge capability, long cycle life, abuse resistance, environmental friendliness, and good safety.[4,12] However, it also shows some disadvantages, such as higher cost than lead acid battery and decreased performance at low temperature.[4] Moreover, there is no significant performance enhancement of it for many years.[12] These features limit its further development.

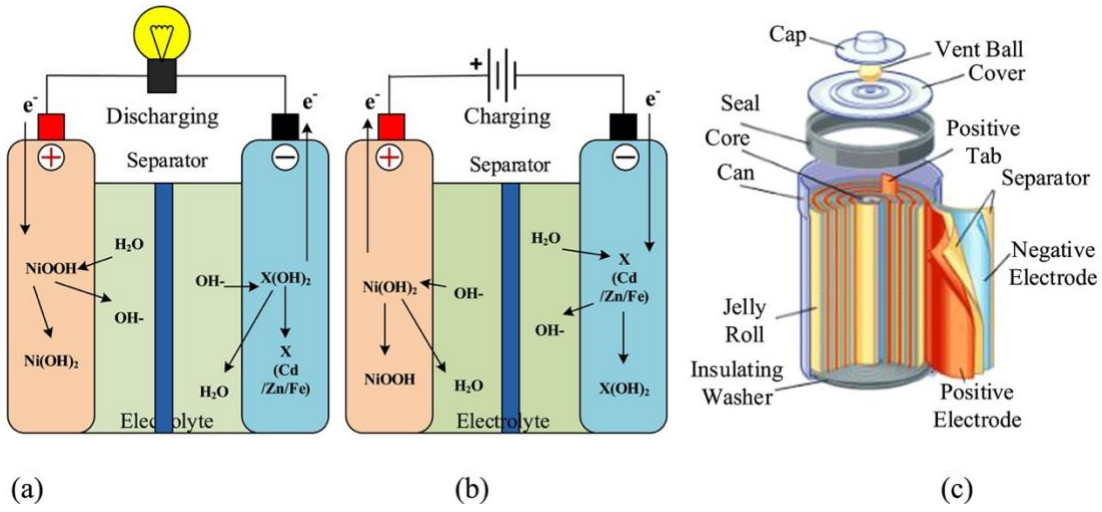

Figure 4 Nickel-based battery chemistry: (a) during discharging, (b) during charging, and (c) battery prototype[9]

Lithium-ion battery (LIB) could be found almost everywhere in people's daily lives. It exists in cellphones, laptops, and even electric vehicles. About 30 years ago Sony Co. commercialized the world's first lithium-ion battery.[13] The cathode materials have been developed and modified since the LIB was first invented. TiS_2, MoS_2, $LiCoO_2$, $LiMnO_2$, $LiFePO_4$, and $LiNi_xCo_yMn_{(1-x-y)}O_2$ are all promising candidates during the development process.[13,14] For the anode research, the carbon-based anode is considered the most promising one because it is reversible with a high capacity (372 mAh/g) and a low reduction potential.[13] The electrolyte is the key component of the LIB. Today's state-of-the-art electrolyte is made of lithium hexafluorophosphate ($LiPF_6$) dissolved in a mixture of cyclic carbonate and linear carbonate.[15] Moreover, the battery chemistry of the discharging and charging process is shown in Figure 5 below, as well as the cylindrical view of the LIB. For example, the overall charge reaction is listed below for $C/LiCoO_2$

battery. The cathode material $LiCoO_2$ will be oxidized to $Li_{(1-x)}CoO_2$, and the anode material carbon will be reduced to LiC_6.[16]

$$LiCoO_2 + 6C \rightleftharpoons Li_{(1-x)}CoO_2 + Li_xC_6$$

Lithium-ion battery has wide applications in portable devices and electric vehicles. It has a high energy density, high columbic and energy efficiency, high-rate and high-power discharge capability, rapid charge capability, and long cycle life.[4] However, it still has some limitations. More specifically, it has a safety concern due to its low thermal-abuse tolerance of electrodes and electrolyte.[17] The extreme conditions such as overcharging, external or internal short circuiting, and high-temperature thermal impacting will cause temperature increase inside the battery and may result in thermal runaway, fire or even explosion.[17,18] Therefore, the effective control of safety issue becomes very critical in LIB systems.

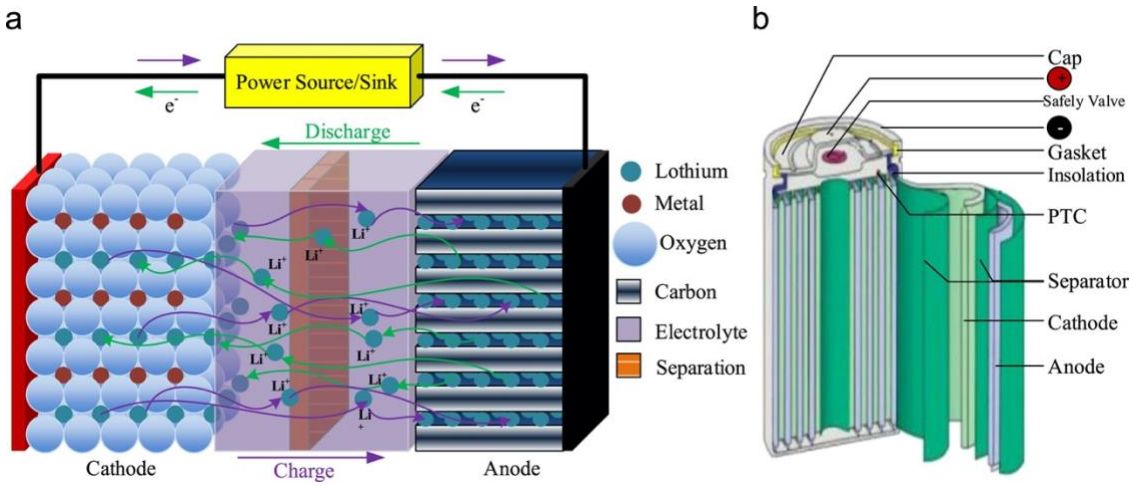

Figure 5 Lithium-ion battery chemistry: (a) during discharging and charging, and (b) cylindrical view of LIB[9]

Therefore, after reviewing various types of batteries on the market, safer, cheaper, less toxic, and high-energy density batteries are in high demand now and in the future.

1.2 Aqueous Rechargeable Zinc Ion Batteries (ARZBs)

Aqueous zinc batteries (AZBs) have a long history of development and commercialization.[19] They are initially researched and developed as a primary cell in 1799 by Alessandro Volta.[20] Afterwards, making AZBs rechargeable have also been a century-long effort since Edison's invention of the rechargeable zinc-nickel (Zn-Ni) battery system began in 1901.[4,21] In the 1970s and 1980s, many studies were reported on understanding the battery mechanism and improving the reversibility of Zn anode and various cathodes.[22] Although these attempts did not successfully make AZBs rechargeable in practical, but they open a good start for the fundamental understanding of battery mechanism.[19] Recently, rechargeable AZBs have been well and further developed by modifying electrode, changing electrolyte with the fundamental understanding of batteries mechanism.[23,24] Then, they become the aqueous rechargeable zinc ion batteries (ARZBs). A schematic of the chemistry inside ARZBs is shown below in Figure 6. The specific mechanism will be discussed in later section.

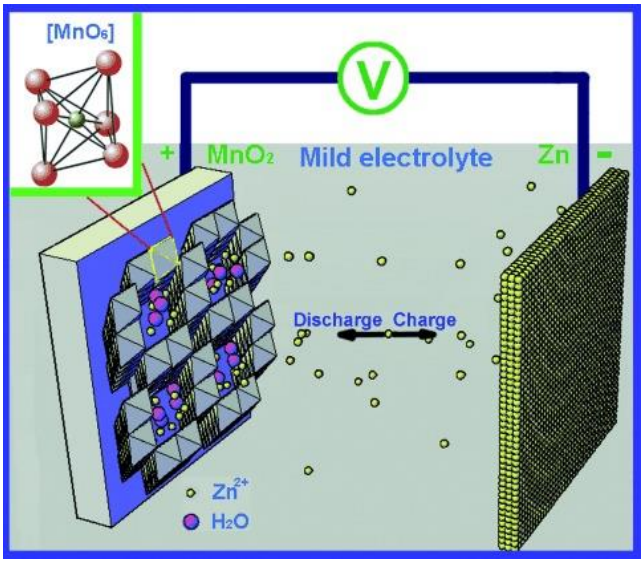

Figure 6 A Schematic of the chemistry inside ARZBs[25]

ARZBs are consist of common components like all other batteries, including cathodes, anodes, electrolyte, current collectors, separators, and packing cases.[19] However, metal zinc anode and water electrolyte have significant advantages in terms of energy, power, safety, cost, and environment.[19] More specifically, ARZBs have attracted many researchers' attention due to the high capacity of zinc (820 mAh/g), low reduction potential (-0.76 V *vs.* standard hydrogen electrode), high abundance, high safety, high environmental friendless, low cost, and impressive electrochemical stability in water due to a high overpotential for hydrogen evolution.[24]

One of the main advantages of ARZBs compared to LIBs is that ARZBs are highly safe. The electrolyte of ARZBs usually consists of aqueous inorganic solutions, such as $ZnSO_4$, which makes the interior of the battery a non-flammable environment, thus greatly reducing the probability of fire or exploration. However, most of lithium-ion batteries have

organic flammable electrolyte, which can cause safety concerns.[25] Therefore, ARZB has a lower safety risk, and it is a better candidate for safety-first battery requirements.

Another advantage is from the zinc because zinc has a high abundance on earth compared to lithium and other common battery anode materials. According to the abundances of chemical elements in the earth's crust study by A.A. Yaroshevsky in 2005, the zinc and lithium element in earth's crust are 8.3×10^{-3} wt% and 3.2×10^{-3} wt%, respectively.[26] Therefore, zinc is a highly abundant element and will have a better price advantage than lithium, thereby reducing the battery cost.

Moreover, zinc is more environmentally friendly than most of battery materials. Compared with lead, lithium, magnesium, and cadmium, zinc is a nontoxic resource,[25] which has less effect on the environment and organisms on earth. Therefore, zinc is a very low toxic and environmental friendly element,[27] making it an excellent candidate for battery materials.

These advantages make ARZB a promising candidate in highly safe, low cost, and environmentally friendly rechargeable batteries.

1.3 Cathode materials for ARZBs

Cathode is one of the most important components of a battery system. During the discharge process, positive ions (e.g., Zn^{2+} in ARZBs) intercalate into the cathode and generate electrons, which is the most critical process for obtaining an efficient battery system.[24] It is essential that cathode has a stable structure and is easy for Zn^{2+} to enter or leave into its structure, which is the main concern for finding a high-performance cathode

material. Therefore, many studies have been done to find the best cathode material for ARZBs. Developments and research have been widely applied to manganese-based materials, vanadium-based materials, Prussian blue analogues, and organic materials.[28]

Manganese-based materials contain tunnel-based MnO_2 polymorphs (α-MnO_2, β-MnO_2 and γ-MnO_2), layer-based MnO_2 polymorphs (δ-MnO_2) and spinel-based MnO_2 polymorphs (λ-MnO_2 and Mn_3O_4).[24,28] More discussion about their structures and properties will be elaborated in the next section. Vanadium-based materials include V_2O_5, NaV_3O_8, and $Zn_{0.25}V_2O_5{\cdot}nH_2O$, etc.[24] Prussian blue analogues (PBAs) are represented by the formula $A_xM_1[M_2(CN)_6]y\cdot nH_2O$, and it has a face-centered cubic structure. (A) represents mobile alkaline metal ions, and the two metal ions (M_1 & M_2 = Mn, Fe, Co, Ni and Zn) are linked together by cyanide (CN) ligands.[29] Common organic materials are calix[4]quinone, polyanilinecalix (PANI), and poly(benzoquinonyl sulfide) (PBQS), etc.[22]

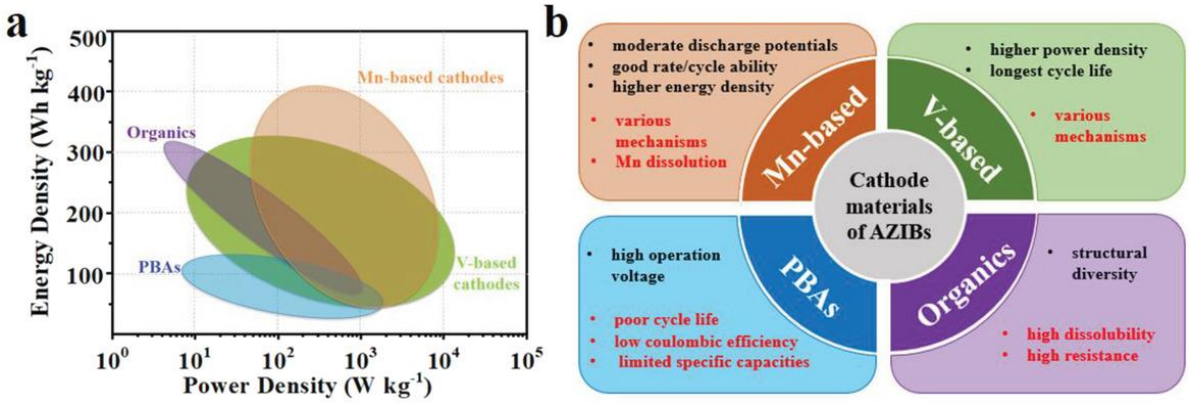

Figure 7 a) Ragone plot of typical representative cathode materials for AZIBs. b) Comparison of the main cathode families in benefits (black) and limitations (red)[28]

Figure 7 shows the energy density, power density, benefits, and limitations of these four types of cathodes. According to the Ragone plot in Figure 7 (a), manganese-based and vanadium-based cathode batteries have higher energy and power density compared to PBAs and organic cathode, especially for the manganese-based cathode batteries, that is also the reason why they are widely developed and studied recently.

A summary table of electrochemical performances of various cathode materials for aqueous zinc-ion batteries is also shown in Table 1 below. It summarizes the potential range (V) and initial discharging capacity (mAh/g) of batteries with different cathodes and electrolytes at various current density. The Mn-based and V-based materials show higher capacity than PBAs and organic cathode in general, which is their advantage and could also be the reason why researchers are studying them.

However, all of them have advantages and limitations. A summary of the benefits and limitations of these four types of cathodes is shown in Figure 7 (b) above. Mn-based cathodes have moderate discharge potential, good rate and cycle ability, and higher energy density, but it suffers from manganese dissolution into electrolyte, and there are various mechanism explanations.[28] V-based cathodes have higher power density and excellent cycling performance, but they have lower operation voltage and specific capacity with various mechanisms. PBAs can provide high operation voltage, but the poor cycling performance, low columbic efficiency, and limited specific capacities limit its further development.[28] Recently, organic cathodes have remarkable performance in cycling performance due to their structural diversity, but the high dissolubility and resistance need to be further investigated.[30]

Table 1 Summary of electrochemical performances of various cathode materials for aqueous zinc-ion batteries[24]

Cathode material	Electrolyte	Potential range (V)	Initial discharge capacity (mA h g^{-1})	Current density (mA g^{-1})
MnO_2	$ZnSO_4$	1.0–1.9	187	100
α-MnO_2	$Zn(SO_4)_2$ + $MnSO_4$	0.8–1.9	405	150
α-MnO_2	$ZnSO_4$	1.0–1.8	233	83
α-MnO_2@C	$ZnSO_4$	1.0–1.8	272	66
α-MnO_2/CNT	$ZnSO_4$ + $MnSO_4$	1.0–1.9	665	100
γ-MnO_2	$ZnSO_4$	1.0–1.8	285	50
β-MnO_2	$ZnSO_4$	1.0–1.8	270	100
δ-MnO_2	$ZnSO_4$	1.0–1.8	122	83
λ-MnO_2	$ZnSO_4$ + $MnSO_4$	0.8–1.9	122	100
Todorokite MnO_2	$ZnSO_4$	0.7–2.0	98	50
Mn_2O_3	$ZnSO_4$ + $MnSO_4$	1.0–1.9	78	100
Mn_3O_4	$ZnSO_4$	0.8–1.9	232	200
$NaMnO_2$	$Zn(CH_3COO)_2$ + CH_3COONa	1.0–2.0	60	120
ZnHCF	$ZnSO_4$	−0.2 to 1.2	73.7	300
ZnHCF@MnO_2	$ZnSO_4$	1.4–1.9	118	100
CuHCF	$ZnSO_4$	0.0–1.1	56	20
NiHCF	$Zn(ClO_4)_2$ in acetonitrile	0.6–1.8	55.6	60
$Zn_{0.25}V_2O_5 \cdot nH_2O$	$ZnSO_4$	0.5–1.4	282	300
$Ca_{0.25}V_2O_5 \cdot nH_2O$	$ZnSO_4$	0.6–1.6	340	60
$CaV_6O_{16} \cdot 3H_2O$	$Zn(CF_3SO_3)_2$	0.2–1.6	367	50
$Mg_{0.34}V_2O_5 \cdot nH_2O$			353	100
$Li_xV_2O_5 \cdot nH_2O$	$ZnSO_4$	0.4–1.4	407.6	1000
$H_2V_3O_8$	$Zn(CF_3SO_3)_2$	0.2–1.6	423.8	100
$H_2V_3O_8$/graphene	$Zn(CF_3SO_3)_2$	0.2–1.6	394	100
$V_2O_5 \cdot nH_2O$/graphene	$Zn(CF_3SO_3)_2$	0.2–1.6	381	60
V_2O_5	$ZnSO_4$	0.4–1.4	224	100
V_2O_5	LiTFSI/$Zn(CF_3SO_3)_2$	0.2–1.6	238	50
$V_6O_{13} \cdot nH_2O$	$Zn(CF_3SO_3)_2$	0.2–1.4	395	100
$NH_4V_4O_{10}$	$ZnSO_4$	0.4–1.4	380.3	100
$Zn_2V_2O_7$	$ZnSO_4$	0.4–1.4	248	50
$Zn_3V_2O_7(OH)_2 \cdot 2H_2O$	$ZnSO_4$	0.2–1.8	213	50
$NaV_3O_8 \cdot 1.5H_2O$	$ZnSO_4$/Na_2SO_4	0.3–1.3	380	50
VO_2	$Zn(CF_3SO_3)_2$	0.7–1.7	265	100
VO_2(B)	$Zn(CF_3SO_3)_2$	0.3–1.5	357	100
rGO/VO_2	$Zn(CF_3SO_3)_2$	0.3–1.3	276	100
VS_2	$ZnSO_4$	0.4–1.4	190.3	50
$Na_3V_2(PO_4)_3$	$Zn(CH_3COO)_2$	0.8–1.7	97	50
$Na_3V_2(PO_4)_2F_3$@C	$Zn(CF_3SO_3)_2$	0.8–1.9	75	80
Mo_6S_8	$ZnSO_4$	0.25–1.0	79	45
$ZnMo_6S_8$	$ZnSO_4$	0.25–1.0	57	128
Calix[4]quinone	$Zn(CF_3SO_3)_2$	0.2–1.8	335	20
1,4-Bis(diphenylamino)benzene	LiTFSI/$Zn(CF_3SO_3)_2$	0.6–2.0	125	26
P-$NiCo_2O_{4-x}$	KOH + $Zn(CH_3COO)_2$	1.4–2.0	309.2	6000
MoS_{2-x} nanosheets	Zinc trifluoromethanesulfonate	0.2–1.2	128.23	100

1.4 Zn-MnO_2 system

Manganese dioxide cathode has been widely studied and developed in ARZBs system because of its high specific capacity, high abundance, low cost and environmental benignity.[19,31] The MnO_2 has various polymorphs with different structure and properties, and they could be classified into three types: tunnel-based, layer-based, and spinel-based MnO_2.[24] Tunnel-based MnO_2 polymorphs have many types with different tunnel size, such as α-MnO_2, β-MnO_2, and γ-MnO_2. α-MnO_2 is a hollandite-type MnO_2 with 2×2 tunnel, β-MnO_2 is a pyrolusite-type MnO_2 with 1×1 tunnel, and γ-MnO_2 consists of both 1×1 and 1×2 tunnels.[24] These tunnel structures allow Zn^{2+} intercalation /deintercalation during the discharge/charge process, which is the main reaction and contributes most to the capacity of the battery.[31] The layer-based MnO_2 polymorph is δ-MnO_2, which is formed by arranging MnO_2 octahedra into sheets through edge sharing. The spinel-based hausmannite structure λ-MnO_2 doesn't have tunnels or layers, instead it has a close packed structure where tetrahedral and octahedral sites are occupied by Mn^{2+} and Mn^{3+}. The crystal structures of these polymorphs are shown below in Figure 8.

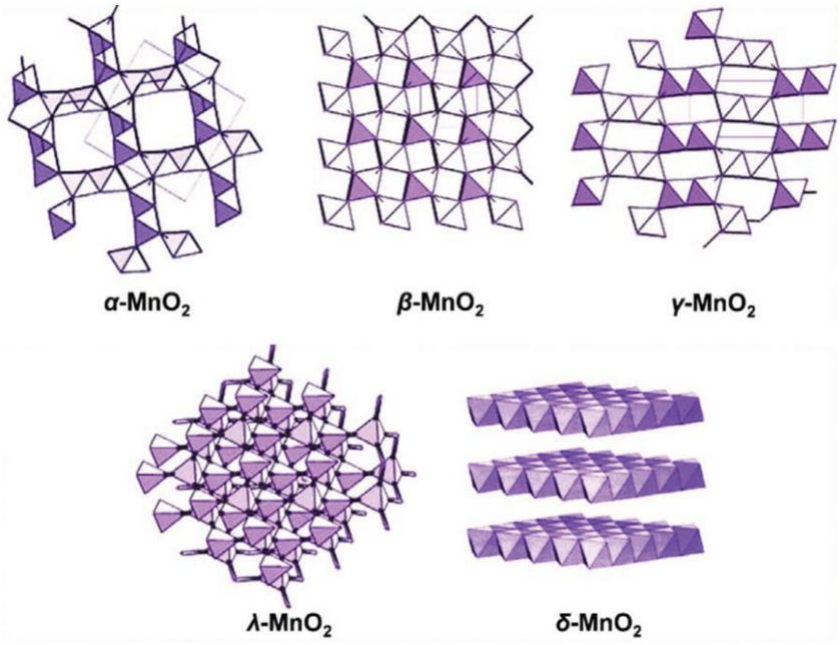

Figure 8 Crystal structures of α-, β-, γ-, λ-, and δ-MnO_2[28]

1.4.1 Storage mechanism of aqueous rechargeable Zn-MnO_2 battery system

The mechanism of the aqueous rechargeable Zn-MnO_2 battery has been investigated by many researchers, however the mechanism is complex and still inconclusive. Three types of energy storage mechanism were commonly reported, consisting Zn^{2+} intercalation /deintercalation into/from MnO_2,[25,32,33] transformation between MnO_2 and MnOOH,[23,31] and co-intercalation of Zn^{2+} and H^+ into MnO_2.[33] The Zn^{2+} intercalation /deintercalation reaction function is shown below.[34] After intercalation, the cathode will become Zn_xMnO_2, and there will be $2x$ electrons gained by the cathode during the reaction.

$$MnO_2 + xZn^{2+} + 2xe^- \rightleftharpoons Zn_xMnO_2$$

The transformation reaction between MnO_2 and MnOOH is also shown below.[34] The MnO_2 will gain one electron and react with one proton to form MnOOH.

$$MnO_2 + H^+ + e^- \rightleftharpoons MnOOH$$

The third type of reaction is shown below as well. The H^+ leads to the Mn^{2+} dissolution, and the increased OH^- forms a complex compound $Zn_4(OH)_6(SO_4) \cdot 5H_2O$.[31]

$$3MnO_2 + 8Zn^{2+} + 2\,SO_4^{2-} + 16\,H_2O + 6e^- \rightarrow 3Mn^{2+} + 2Zn_4\,(OH)_6(SO_4) \cdot 5H_2O \downarrow$$

The anode reaction is that zinc loses two electrons to form Zn^{2+}, and the reaction function is shown below:

$$Zn \rightleftharpoons Zn^{2+} + 2e^-$$

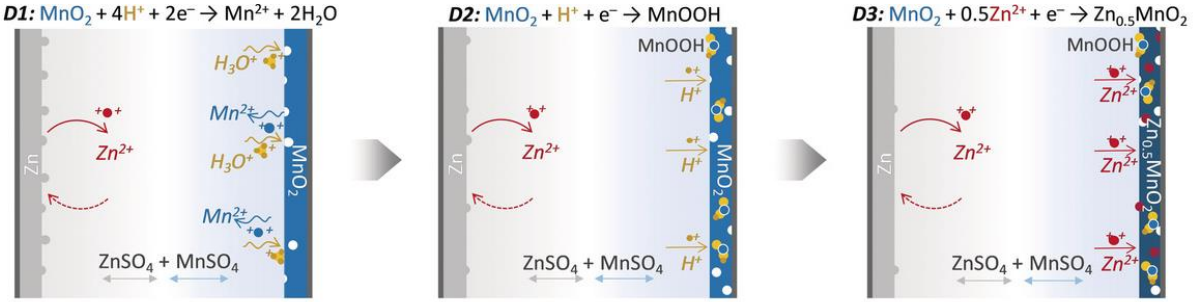

Figure 9 Schematics and energy storage mechanisms of Zn/MnO_2 battery[35]

There is also a study done by Qiao et al. in 2019.[35] As shown in Figure 9 above, they illustrated the rection mechanism at different discharge voltage. The D1 region is between 2.0 V and 1.7 V, D2 is 1.7V to 1.4 V, and D3 is 1.4V to 0.8 V. At different voltages, the reaction mechanism varies. In D1 region, the Mn^{2+} dissolution reaction is the main contributor to the capacity. In D2 region, the formation of MnOOH contributes most to the capacity. In D3 region, the Zn^{2+} intercalation /deintercalation reaction is the main reaction.

Therefore, the specific reaction mechanism needs to be further investigated in different Zn-MnO_2 system and conditions, and researchers need to pay more attention when doing research at various voltage, current, electrolyte, and phases of MnO_2.

1.4.2 Advantages and limitations of aqueous rechargeable Zn-MnO_2 battery system

The aqueous rechargeable Zn-MnO_2 system has attracted many researchers' attention and been widely developed because of its high theoretical capacity, high safety, high abundance, low cost, and environmental friendliness. The battery capacity could be calculated by Faraday's law, and the calculation process of the theoretical capacity of Zn and MnO_2 is shown below separately. The n represents for the moles of electrons of half reaction, F is the Faraday constant (96,485 C/mol), and Mw is the molecular mass of the cathode or anode material.[4]

$$Q = \frac{n \cdot F}{3600 \times Mw}\ Ah/g$$

$$Q(Zn) = \frac{n \cdot F}{3600 \times Mw}\ \frac{Ah}{g} = \frac{2 \times 96485\ \frac{\mathrm{A \cdot s}}{\mathrm{mol}}}{3600\ \frac{s}{h} \times 65.38\ \frac{g}{mol}} = 820\ mAh/g$$

$$Q(MnO_2, 1\ e^-) = \frac{n \cdot F}{3600 \times Mw}\ \frac{Ah}{g} = \frac{1 \times 96485\ \frac{\mathrm{A \cdot s}}{\mathrm{mol}}}{3600\ \frac{s}{h} \times 86.94\ \frac{g}{mol}} = 308\ mAh/g$$

$$Q(MnO_2, 2\ e^-) = \frac{n \cdot F}{3600 \times Mw}\ \frac{Ah}{g} = \frac{2 \times 96485\ \frac{\mathrm{A \cdot s}}{\mathrm{mol}}}{3600\ \frac{s}{h} \times 86.94\ \frac{g}{mol}} = 616\ mAh/g$$

Therefore, the maximum theory capacity of the Zn-MnO_2 battery is 616 mAh/g if the cathode MnO_2 only have two electron transfer reaction. In reality, the cathode usually has different reactions with charge transfer of both 1 e^- and 2 e^-, so the theoretical capacity will be generally between 308 mAh/g and 616 mAh/g, which is a relatively high theoretical capacity compared to other batteries in the market.

The aqueous inorganic electrolyte of the Zn-MnO_2 battery makes it much safer than other organic flammable electrolyte batteries, such as most of lithium-ion batteries. Moreover, the zinc and manganese dioxide are both high abundant, low cost, and environmentally friendly compared to other electrodes.[36] These advantages make the aqueous rechargeable Zn-MnO_2 battery system more competitive in the battery market.

However, the aqueous rechargeable Zn-MnO_2 battery usually suffers from the Mn dissolution and zinc dendrites formation problems during the charge/discharge process.[27,36–40] More specifically, during the cycling process, there will be some structural conversion and disproportionation reaction of the Mn cathode, which could cause the contraction of both the capacity and the cycling performance.[41] At first, the MnO_2 will react with H^+ to form Mn^{2+}, a reaction equation is shown below.

$$MnO_2 + 4H^+ + 2e^- \rightleftharpoons Mn^{2+} + 2H_2O$$

This reaction will cause pH increase, and then the OH^- will combine with Zn^{2+} and H_2O to form a precipitation of zinc hydroxide sulfate ($Zn_4(OH)_6(SO_4)\cdot xH_2O$),[42] which can decrease the cyclability of the whole system.

$$4Zn^{2+} + SO_4^{2-} + (x+6)H_2O \rightarrow Zn_4(OH)_6(SO_4)\cdot xH_2O \downarrow + 6H^+$$

Another common problem in ARZBs is the zinc dendrite formation during the cycling process. Since commercial Zn foil is generally used directly in experiments, the zinc surface will have small protuberances that could be charge centers, accumulating charges and causing dendrites to grow on the surface.[43] Even though the zinc surface is smooth by treatment, there are still some defects on the surface of the zinc foil during the non-homogeneous zinc stripping and plating reactions,[36] which may prick the separator and

cause a short circuit.[44] Figure 10 elaborates the formation and growth mechanism of zinc dendrites in ARZBs. After the continuous formation and growth of zinc dendrites, the separator may be stabbed by zinc dendrites in the end. In addition, some side reactions may occur during the cycling process, such as the evolution of H_2 and the formation of inactive substances, which can reduce the electrochemical kinetics of ARZBs and cause capacity decay.[36] Strategies to overcome these problems will be discussed in the next section.

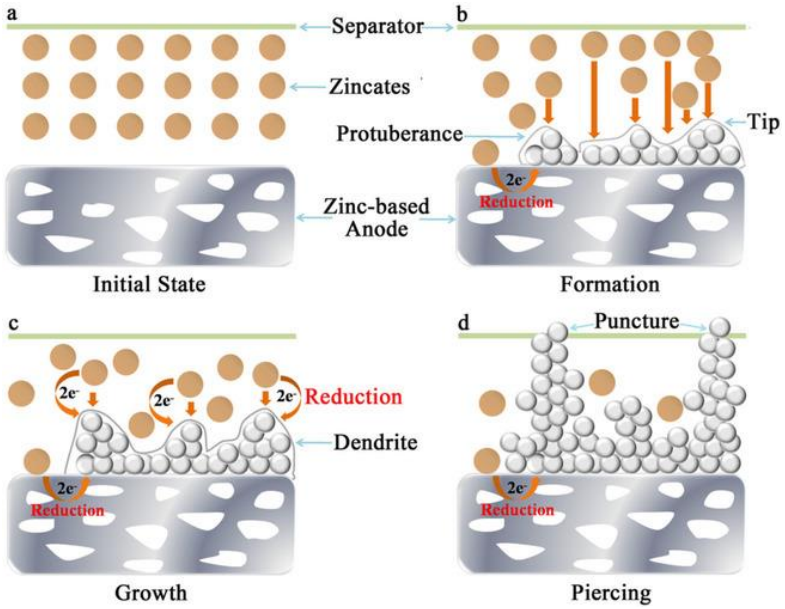

Figure 10 The formation and growth mechanism of zinc dendrites in ARZBs[45]

1.4.3 Strategies to overcome limitations of aqueous rechargeable Zn-MnO_2 battery system

Many attempts have been tried to overcome the Mn dissolution and zinc dendrites formation problems as shown in Figure 11 below. For example, the Mn dissolution problem could be controlled by designing and changing the structure of cathode, surface coating on cathode, and adding additives into the electrolyte.[41] The MnO_2 cathode structure might

change during the cycling process, so a stable and reliable MnO_2 tunnel structure is very critical for a long cycle-life battery. Liang et al. reported a method of adding K^+ into MnO_2 tunnel to form $K_{0.8}Mn_8O_{16}$, which can bind to Mn polyhedrons and effectively inhibit the Mn dissolution.[46] A high energy density of 398 Wh/kg and a long cycle life of 1000 without significant capacity fading were obtained, offering great potential for ARZBs.

Surface coating is also a very effective method to control the Mn dissolution because it could stabilize the cathode structure and provide a protective layer for active material in battery systems. For example, Wu et al. published a graphene scroll coated MnO_2 cathode in 2018, and this approach greatly reduced the dissolution of cathode and improved the electrical conductivity and capacity of the system.[47] More specifically, the battery can deliver a high capacity of 362 mAh/g at 0.3 A/g after 100 cycles, and it also showed excellent cycling performance of 3000 cycles with 94% capacity retention, which is a great improvement for ARZBs.[47]

Another efficient way to manage the Mn dissolution is to add additive ions into the electrolyte. The most common method is to pre-add Mn^{2+} into the electrolyte to stabilize the crystal structure of MnO_2 and limit the Mn vacancies during the Zn^{2+} insertion process, which is because excessive Zn^{2+} ion insertion can lead to poor capacity retention and instability of the crystal structure.[48] Pan et al. reported a method in 2016 of adding $MnSO_4$ into the electrolyte, and the battery capacity can keep 92% after 5000 cycles, which is a highly reversible ARZB system and it provides great potential for the further development of ARZBs.[23]

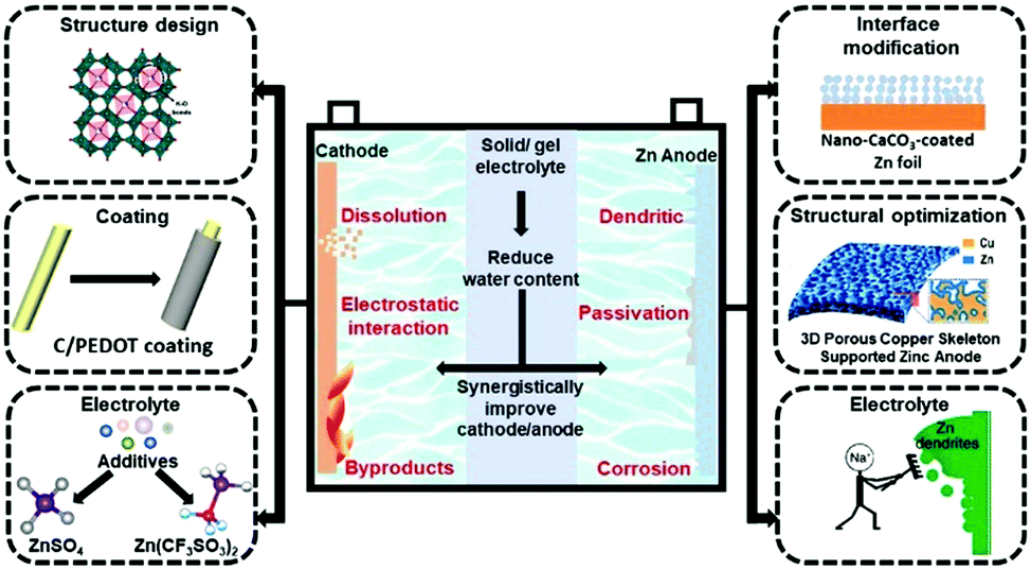

Figure 11 Challenges and optimization strategies in aqueous ZIBs system[41]

The zinc dendrites formation issue could be solved by surface modification of the zinc foil, structure optimization of the anode, and modifying the electrolyte by adding other metal ions.[41] Surface modification method is a common method to control the zinc dendrite formation. Carbon black, nanoporous $CaCO_3$,and TiO_2 are all effective surface coating to obtain flat nanocrystal deposited layers instead of coarse crystals or zinc dendrite growth.[36,41,49] For example, Wang et al. reported a carbon black coating method on zinc foil in 2020, which could significantly improve the cyclability to 1000 cycles with 87.4% capacity retention compared to 42.6% capacity retention without surface modification.[36] Another example is that Zhao et al. addressed a ultrathin TiO_2 coating on zinc in 2018. The coating layer acts as a stable passivation layer to avoid direct contact between the zinc foil and the electrolyte, thus controlling the zinc dendrites growth and H_2 evolution. As a result, the batter cyclability was improved to 1000 cycles with 85% capacity retention.[49]

Structural optimization of the Zn anode is also an effective and popular way to control the zinc dendrites growth. Among them, designing 3D electrode is the most common method because it can provide a higher surface area, more active sites for ions, and enhance the permeability of the electrode.[50] More specifically, carbon cloth deposition, graphite felt wafers, and porous copper skeleton are all efficient designs. For instance, the 3D porous copper skeleton zinc anode showed increased energy and power density, fast electrochemical kinetics, and improved cycling stability, which exhibited a high capacity of 364 mAh/g.[51]

Electrolyte optimization is a another very useful and efficient approach to reduce zinc dendrites growth. There are methods including pre-addition of relevant salts, concentration adjustment, addition of organic solvents, and introduction of surfactants to both suppress the zinc dendrites and control the Mn dissolution.[41] For example, Zeng et al. investigated a method to add acetate ions into the electrolyte, which can not only provide a dendrite-free zinc anode with high columbic efficiency, but also let the Mn dissolution reaction revisable and increase its capacity.[39]

The above is a brief overview of strategies to overcome the limitations of ARZBs system. They are all efficient methods and can bring new ideas for future research.

1.5 Gelatin

Gelatin is a non-toxic and biodegradable water-soluble functional protein with high interest and value,[52] and it is also known as hydrolyzed collagen or collagen peptides. It is usually partial hydrolysis from collagen of animal body parts, such as skin, bone, and tendon.[52] The hydrolysis process is shown in Figure 12 below. When collagen is

hydrolyzed under heat, the triple helix will detach into three polypeptide chains to form a gelatin solution.[53] Afterwards, when the gelatin solution is cooled under 35 °C, the polypeptides chains will aggregate together and reform the random triple helices, which is called junction zone, and these junction zones act as crosslinks to form the gelatin networks as a gel.[53]

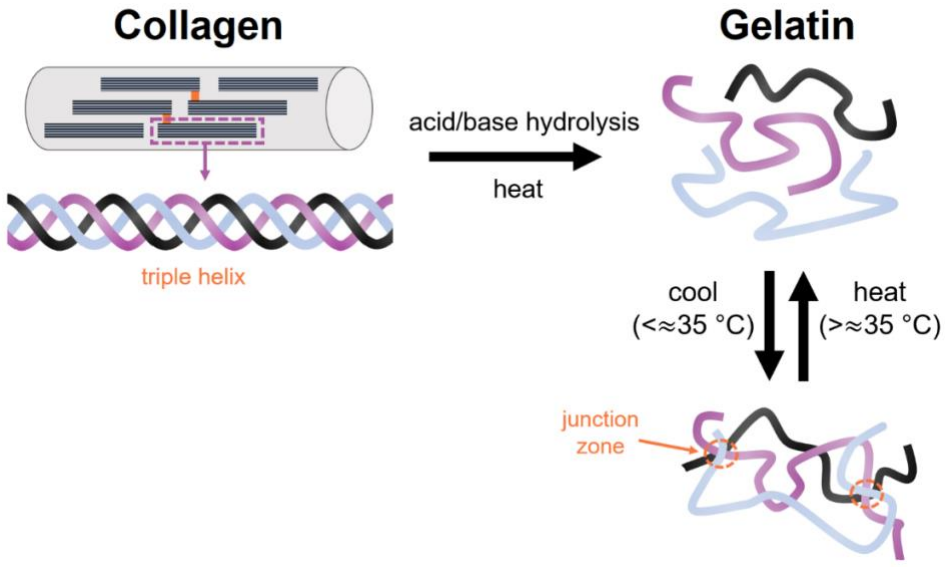

Figure 12 Hydrolysis process of collagen to produce gelatin[53]

Gelatin is reported to be consisted of eighteen amino acids, which are linked together in a partially ordered manner. The basic chemical structure of gelatin is shown below in Figure 13. The gelatin is a heterogeneous mixture of single or multi-stranded polypeptides, and each helix contains 300 to 4000 amino acids.[54] Moreover, there are two types of gelatin based on different manufacture process, Type-A and Type-B. Type-A gelatin is collected by acidic treatment of collagen with an isoelectric point (pI) of 7.0 – 9.0 while Type-B gelatin is obtained through alkaline hydrolysis with a pI between 4.8 and 5.0.[55,56]

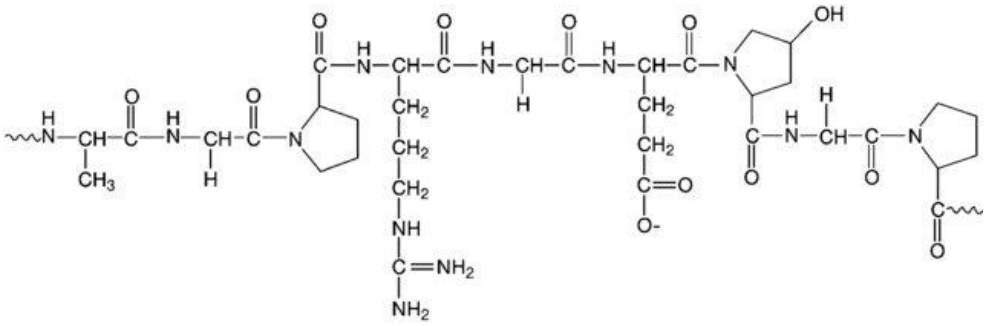

Figure 13 Basic chemical structure of gelatin[54]

Three groups of amino acids are the main components of the gelatin molecule.[52] Glycine and alanine make up nearly one-third to half of the total amino acid residues,[57] proline or hydroxyproline account for about one-fourth of residues, and approximately another one-fourth is the basic or acidic residues.[52] Moreover, it has been reported that tryptophan is an essential amino acid residue in the gelatin molecule.[58] A summary of the amino acid composition of gelatin is shown below in Figure 14.

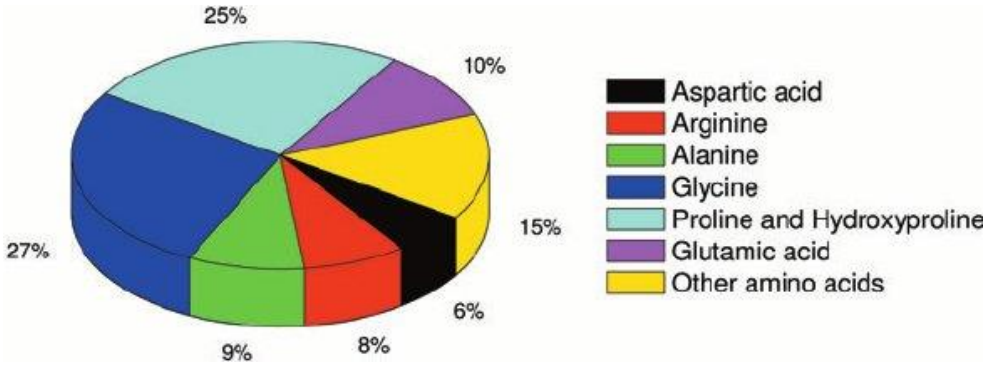

Figure 14 Amino acid composition of gelatin[54]

1.5.1 Properties

Gelatin is classified as a physical gel, and the interactions between peptide chains are hydrogen bonds and van der Waal's force with an E≈2 kcal/mole.[59] The gel strength and melting point are the main physical properties of the gelatin, and they are determined by molecular weight and amino acid composition of the ratio of α/β-chains in the gelatin.[60] More specifically, gelatin with larger molecular weight or more α-chains usually has higher gel strength and melting point.[61] Another important property of gelatin is its film-forming ability. Various research has proven that gelatin has an excellent film forming ability and the film exhibits fabulous protectivity.[59,62,63] For example, Gómez-Guillén et al. found in 2007 that fish gelatin films exhibited lower water vapor permeability (VWP) compared to pigskin gelatin, suggesting a better application of fish gelatin films in encapsulated pharmaceutical and frozen food systems to reduce water loss.[62]

Another essential property of gelatin is its good ionic conductivity. It has been commonly used in solid-state electrolyte batteries and electrodeposition. For instance, Li et al. reported in 2018 that the gelatin-based electrolyte has a good ionic conductivity of 5.68×10^{-3} S cm^{-1} in zinc ion battery system, which is a good ionic conductivity compared with other polymers.[64] The gelatin has also been used in electrodeposition and shows excellent performance. Wu investigated in 2016 that the addition of gelatin can decrease the amount of carbon in alloys during the electrodeposition process because of the adsorption of gelatin through hydrogen bonds and van der Waal's force.[65]

1.5.2 Applications

Gelatin has been widely used in the food industry, including clarifier, stabilizer, emulsifier, thickener, and protective coating material, etc.[52] More specifically, it has been commonly used in jelly, dessert, candy, ice cream, and yogurt, etc.[66] In addition, gelatin also plays an important role in the pharmaceutical industry, such as capsules, tablet coating, ointments, etc.[52] Moreover, it has many applications in batteries and wearable electronics because of its good ionic conductivity and flexibility.

Many gelatin applications in wearable electronics field have been reported so far, and many of them have the solid-state gelatin-based electrolyte because it is safe, wearable and flexible. For example, Li et al. in 2018 fabricated a wearable and rechargeable zinc ion battery with gelatin based hierarchic polymer electrolyte, and it exhibited a high specific capacity of 306 mAh/g and a long cycle life of 1000 cycles with 97% capacity retention, which is an outstanding electrochemical performance for zinc ion batteries.[64] Another example is that Han et al. in 2019 reported an inorganic salt-enhanced gelatin based solid-state electrolyte Zn-MnO_2 battery with a high specific capacity of 285 mAh/g and an excellent cycling performance of 500 cycles with 90% capacity retention.[67] These research all prove that the gelatin based solid-state electrolyte battery is a promising candidate for wearable electronic, and it can have more applications in the future.

The gelatin has also been applied in aqueous rechargeable batteries because it could absorb metal ion through hydrogen bonds, van der Waal's force, and ionic interactions, which can control the Mn dissolution and improve the battery cycling performance.[31] Liu et al. in 2020 reported an bionic electrode microskin composed of gelatin to confine Mn^{2+}

in the cathode to convert the irreversible side reactions into useful and reversible reaction, which can contribute to the battery capacity.[31] A schematic of the electrode microskin is shown below in Figure 15. The battery shows an excellent specific capacity of 415 mAh/g at 20 mA/g and an outstanding cycling performance of 1000 cycles with 90% capacity retention at 500 mA/g, which is a 30% improvement compared with the unmodified cathode.[31] The existence of gelatin significantly controlled the Mn dissolution and stabilized the MnO_2 structure, resulting in a higher capacity and better cyclability.

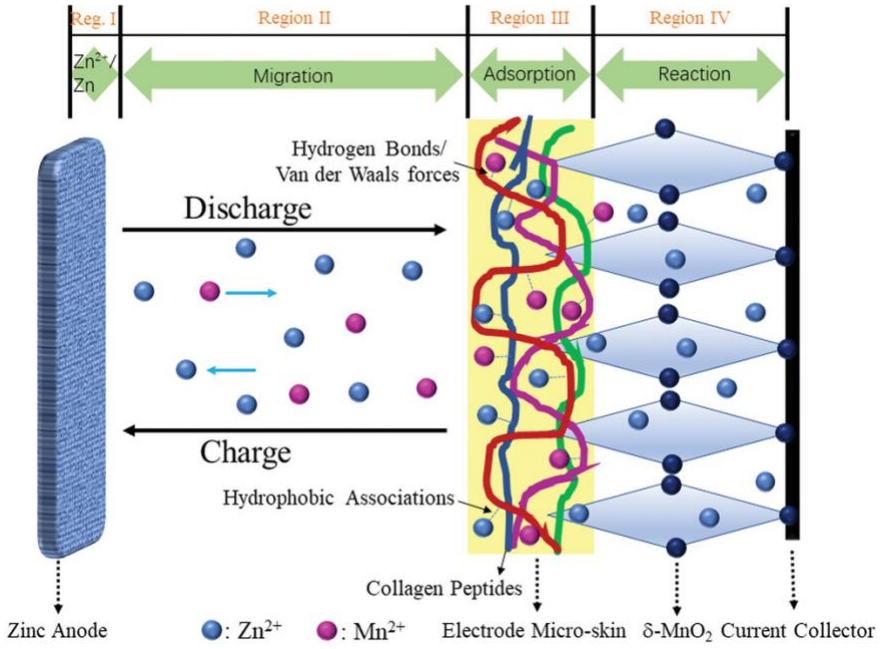

Figure 15 A schematic of the gelatin electrode microskin in aqueous rechargeable Zn-MnO_2 battery system[31]

Therefore, gelatin is a safe, cheap, non-toxic, flexible, and conductive gel with high gel strength. It shows great potential for further applications in the food industry, pharmaceutical industry, wearable electronics, and batteries.

1.6 PEDOT: PSS polymer

Poly(3,4-ethylenedioxythiophene): poly(styrene sulfonate) (PEDOT: PSS) is a conductive polymer mixture of two ionomers: PEDOT and PSS. The PEDOT part has conjugated rings which carries positive charges while the PSS part carries negative charges because of its deprotonated sulfonyl group.[68] In addition, PSS is a polymer surfactant that helps to disperse and stabilize PEDOT in water solutions.[69] The chemical structure of the PEDOT: PSS is shown below in Figure 16. The PEDOT: PSS is a kind of dark blue opaque solution with high conductivity, good stability, and excellent film-foaming properties, which has wide applications in solar cells, batteries, supercapacitors, and fuel cells.

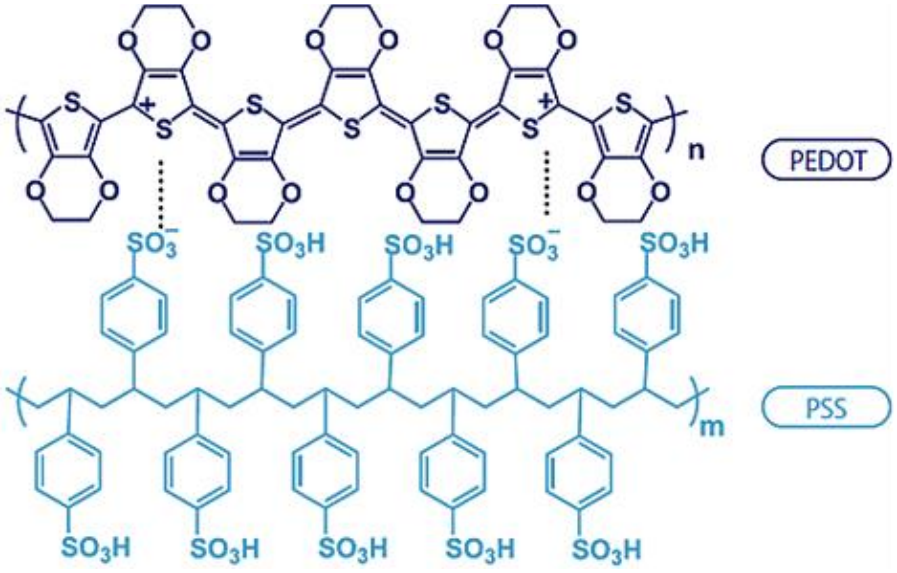

Figure 16 The chemical structure of the PEDOT: PSS[70]

1.6.1 Properties

High conductivity is the one of the main reasons why PEDOT: PSS has such wide applications in energy storage systems. It has a very high conductivity of 300 $S \cdot cm^{-1}$ and a

high work function of 5.0-5.2 eV.[68,69] The excellent conductivity and high working function can trigger spontaneous transitional transfer with fast kinetics, so PEDOT: PSS has catalytic properties as well.[69] The PEDOT: PSS also exhibits excellent thermal stability up to 1000 h at 100 °C in air with no influence in conductivity.[71] The distinguished transparency and film-forming ability of PEDOT:PSS also attract many researchers' attention. PEDOT: PSS could form a uniform and continuous thin film on various substrates through different coating method, such as spin coating, slot die coating, spray deposition, and screen printing, etc.[69] The roughness of the film surface is usually less than 5 nm, which is a very smooth surface compared with other materials.[69] Moreover, the PEDOT: PSS film is essentially transparent in the visible light range, making it have potential applications in electronic devices, including sensors, organic light emitting diodes, and transistors.[72]

1.6.2 Applications

PEDOT: PSS has been widely used in solar cells, batteries, supercapacitors and fuel cells to improve their conductivity and performance. Recently, PEDOT: PSS has been used in heterojunction solar cells (HSCs) by simply spin coating method on n-type silicon substrate because of its easy fabrication process and cost-effective property.[73] Thomas et al. reported a silver nanowire embedded PEDOT: PSS HSC in 2020 with a high power conversion efficiency of 15.3%, which is the highest record in planar single-junction HSCs to date without complex fabrication processes.[74] Therefore, PEDOT: PSS significantly enhanced the performance of solar cells, and it will have more potential applications in the future.

PEDOT: PSS has also been commonly applied in batteries to increase the battery performance. For example, Ko et al. declared a method in 2015 of coating PEDOT: PSS onto Mn_2O_3 nanowires anode in lithium-ion battery system by simple sonicating method.[68] The PEDOT: PSS coated lithium-ion battery showed an excellent specific discharging capacity of 1450 mAh/g after 200 cycles at 100 mA/g, which is due to the reduced surface resistance and protection of electron channels by PEDOT: PSS coating.[68] Another application of PEDOT: PSS is in the flexible solid-state electrolyte batteries. Zeng et al. demonstrated a rechargeable flexible quasi-solid-state Zn-MnO_2 battery in 2017.[75] A schematic of the battery structure is shown in Figure 17 (a), and the morphology of Zn anode and MnO_2@PEDOT cathode are also shown in Figure 17(b), (d), and (e). Benefiting from the PEDOT layer and the addition of Mn^{2+} in electrolyte, the battery exhibits a remarkable capacity of 366 mAh/g and a good cyclability of 300 cycles with 83.7% capacity retention in aqueous electrolyte.[75] Moreover, the battery shows a good cycling performance of 300 cycles with 77.7% capacity retention and a high energy density of 504.9 Wh/kg with PVA/$ZnCl_2$/$MnSO_4$ solid-state electrolyte.[75] Therefore, PEDOT: PSS can improve the battery performance and will have more applications in the future.

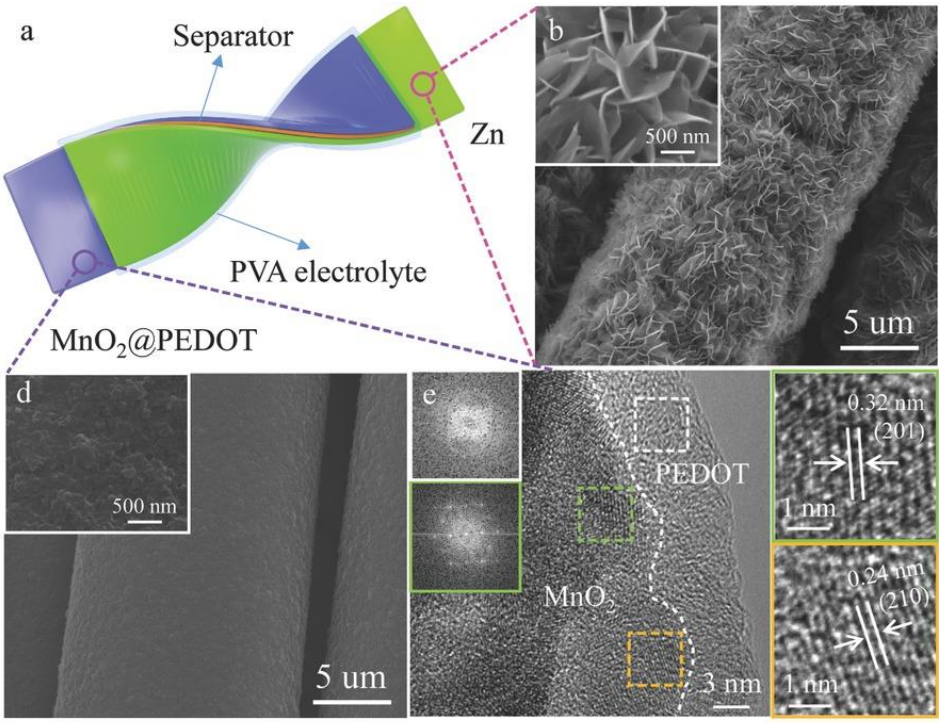

Figure 17 (a) A schematic of the flexible solid-state electrolyte Zn-MnO_2@PEDOT battery; (b) SEM image the Zn anode; (d) SEM images and (e) HRTEM images of the MnO_2@PEDOT sample[75]

1.7 Project Scope and Objectives

Overall, the work in this thesis is based on three main objectives:

1. Synthesize a high capacity and stability ε-MnO_2 material using an innovative, easy, safe, and cost-effective co-precipitation method. The purity and electrochemical performance of the commercial MnO_2 is not satisfying, and hydrothermal method is usually used in laboratory, which is dangerous and hard to control during the reaction process. Therefore, there is a strong demand to synthesize a high purity, high capacity, and high stability MnO_2 material with easy, safe, and cost-effective method both in the lab and industry.

2. Confine the Mn^{2+} inside the cathode and manage the Mn dissolution by using gelatin-coated MnO_2 cathode in aqueous rechargeable Zn-MnO_2 batteries to improve the cyclability of the battery. The Mn dissolution problem is very common in aqueous rechargeable Zn-MnO_2 batteries. The gelatin coating on cathode could confine the Mn^{2+} through hydrogen bonds and van der Waal's force and control the Mn dissolution, resulting in a remarkably improved battery's cycling performance.

3. Control the Mn dissolution and improve the battery cycling performance by using PEDOT: PSS coated cathode in aqueous rechargeable Zn-MnO_2 batteries. The PEDOT: PSS is a highly conductive polymer mixture with negatively charged sulfonyl group that can attract positive metal ions. Therefore, PEDOT: PSS could be coated on top of the MnO_2 cathode to confine Mn^{2+} ions and manage the Mn dissolution effect, causing a significant improvement in the battery's cyclability.

Chapter 2: Characterization Techniques

2.1 Material Characterization Techniques

In this section, the working mechanism and instrument information of material characterization techniques will be introduced, including scanning electron microscope (SEM), X-ray diffraction (XRD), Fourier transform infrared spectroscopy (FTIR), and X-ray photoelectron spectroscopy (XPS).

2.1.1 Scanning Electron Microscope (SEM)

Scanning electron microscope (SEM) is a versatile electron microscope available for the detection and characterization of the surface morphology and chemical composition of the sample with the scale of nanometer. As shown in Figure 18, an SEM setup consists of four major components, including electron gun (also called electron source), condenser lenses, scan coils, and electron detectors. When operating an SEM, electrons produced from an electron gun pass through a combination of condenser lenses and aperture to form a focused and narrowed electron beam.[76] The beam goes through a pair of scan coils that are used to control the position of the electron beam onto the sample, then hits the surface of the sample, which is mounted on a platform in the sample holder.[76] As a result of the interaction between the electron beam and the sample, several signals are generated and recorded by an applicable detector.[76]

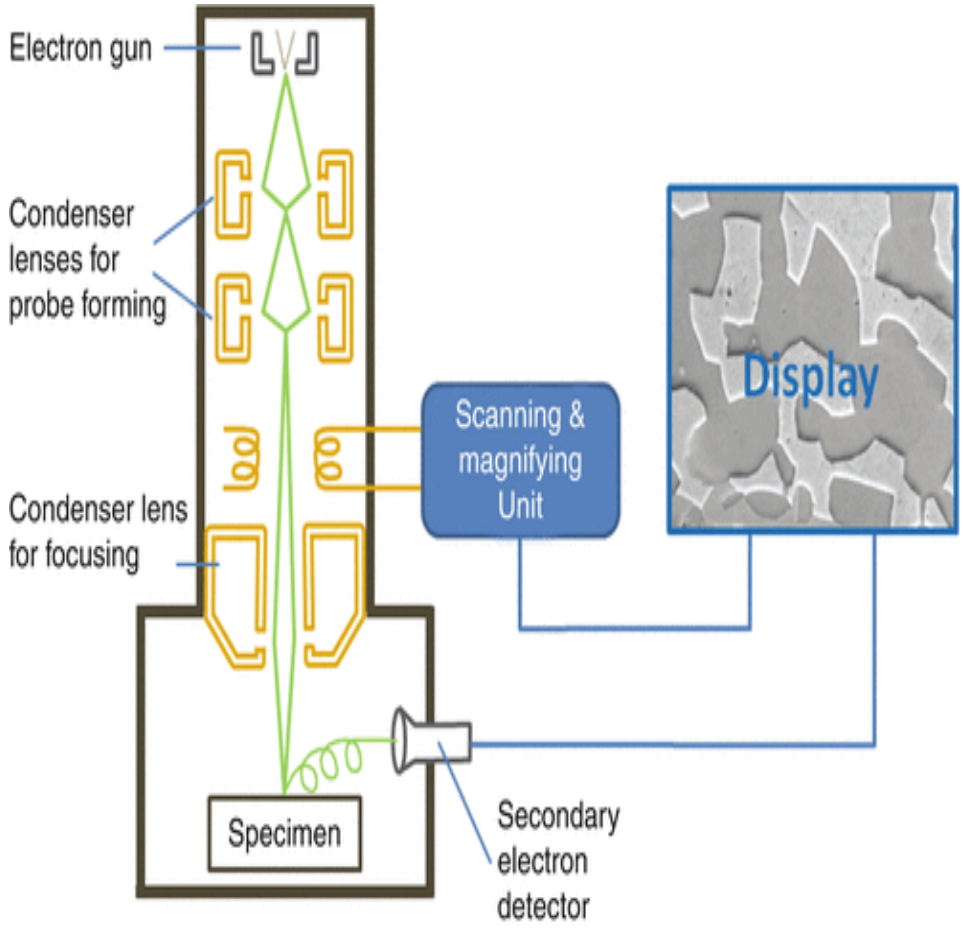

Figure 18 A schematic of the scanning electron microscopy with main components[77]

There are three key applications performing on an SEM implement, including secondary electron imaging, backscattered electron imaging, and energy dispersive X-ray (EDX) spectroscopy. Secondary electrons imaging is mainly useful to showcase for surface morphology and topography. Secondary electrons are created by the ionization of specimen atoms colliding with incident electron beam, and these secondary electrons have relatively low kinetic energy that is usually less than 50 eV.[77] In light of the limited energy, secondary electrons could be only released and imaged from the surface, exhibiting the surface morphology and topography.[78] Backscattered electrons retain almost all the energy carried

by the incident electrons, thus have higher kinetic energy compared with backscattered electrons.[77] Based on the fact that the yield of backscattered electrons has a linear relationship with the atomic number of the element, taking advantaging of backscattered electrons in imaging can help to assess the elemental distribution at the surface of the specimen.[77] Moreover, backscattered electrons can also be used in crystal analysis due to the high sensitivity of backscattered electron yield and scattering angle to the crystal structure.[77] Energy dispersive X-ray spectroscopy is an important characterization on SEM to analyze the composition of a sample on the basis of characteristic X-ray emission.[78] X-ray photon is emitted as a result of high-energy outer shell electrons demote to low-energy vacant level.[78] The frequency of these photons can be detected and collected by the detector, therefore by using this information, types of elements and their relative contents can be identified and evaluated.[78]

In this work, SEM measurement was used to detect the morphology and structure of cathode materials. And all samples were performed on a Zeiss Leo FESEM 1530 with a 10 kV of accelerating voltage in vacuum.

2.1.2 X-ray Diffraction (XRD)

X-ray diffraction (XRD), an accurate and rapid analytical technique, utilizes X-rays to investigate and identify the crystal structure and phase information, as well as reveal the dimensions of unit cells. Because of these specific features, XRD plays a vitally important role in determining an unknown sample in the field of material science, biology, geology, and engineering. X-ray diffractometer is made up of three major parts shown in Figure 19, an X-ray source which is normally from an X-ray tube, a sample holder, and an X-ray

detector.[79] X-rays generated by a cathode ray tube are collimated and directed towards the solid sample mounted on the sample holder.[79] As a result, a portion of X-rays are absorbed by the sample, rest portions of rays are scattered and reflected.[80] As the sample and detector rotate, the signals of reflected X-rays are captured and recorded for each set rotation.[80] When the geometry of X-ray signals satisfies the Bragg Equation, a peak in intensity occurs and is collected by an X-ray detector.[81]

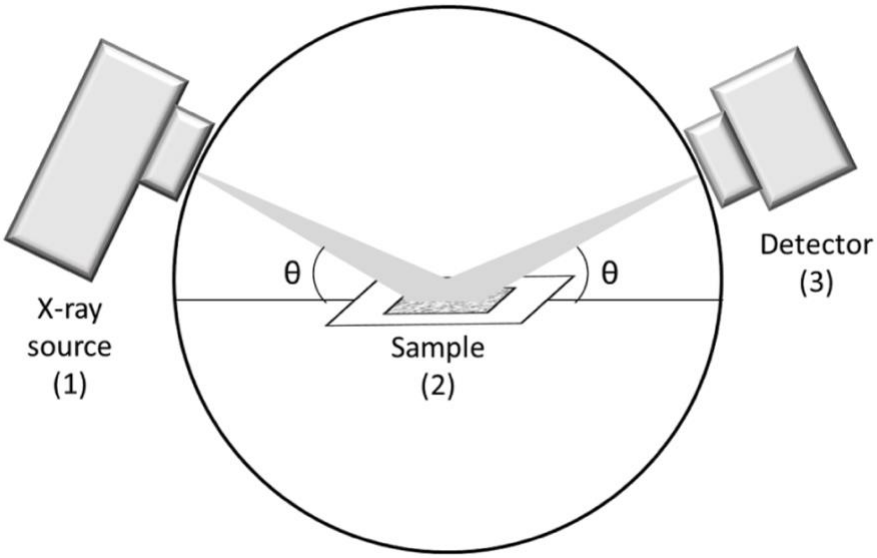

Figure 19 A schematic of the X-ray diffraction equipment[79]

Moreover, the constructive inference will be produced when the interaction between X-rays and the sample fulfils Bragg's law, and the equation is shown below:

$$n\lambda = 2d \sin\theta$$

Where n is an integer, λ is the wavelength of incident X-ray, d is the distance of lattice planes, and θ is the angle between incident X-ray and lattice plane.[80] Once the distance between the lattice planes are determined, the Miller index for that particular lattice plane can be calculated by using the following equation:

$$d = \frac{a}{\sqrt{\sqrt{h^2 + k^2 + l^2}}}$$

where a refers to the length of unit cell and h, k, and l refer to the Miller indices affiliated with the particular lattice plane.[80]

Additionally, XRD measurement can also determine the crystallite size of the sample by using Scherrer equation:

$$L_{hkl} = \frac{K\lambda}{\beta \cos(\theta)}$$

Where L_{hkl} is the size of the crystallite, K is a Scherrer shape factor, and β is the full width at half-maximum (FWHM) of the corresponding peak.[82]

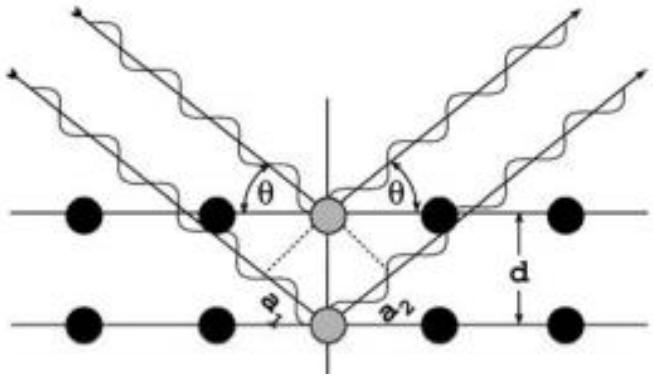

Figure 20 Illustration of the Bragg's diffraction[80]

In this work, the crystal structure of MnO_2 was determined by using a Bruker D8 Discover X-ray diffractometer with a copper target and monochromatic Cu-Kα radiation with the wavelength of 1.54 Å. The XRD patterns were recorded from the range between 20° and 80° with a scan rate of 0.02 degree per second.

2.1.3 Fourier Transform Infrared Spectroscopy (FTIR)

Fourier transform infrared spectroscopy (FTIR) is a technique to collect optical properties such as absorption and transmission of materials in the infrared range, which is widely used in identifying unknown materials, including organic, inorganic, and polymeric chemicals with the utilization of infrared beam. When infrared light having longer wavelength and lower frequency compared with visible light passes though the sample, some of the radiation with certain wavelength is absorbed by the sample and the rest is transmitted through the sample. The transmitted radiation is collected by a detector and the signal revealed at the detector represents a certain molecular fingerprint for different molecules, which can be analyzed to identify the types of organic and/or inorganic chemical structures.[83]

An FTIR spectrometer includes an IR source, interferometer, sample cell, amplifier, A/D convertor, and detector. Among these different components, an interferometer is the core one in the FTIR spectrometer. As shown in Figure 21, infrared light generated in an IR source reaches a partially coated mirror and then half of the radiation is reflected, and the remaining half is transmitted. The resulting two beams following Path 1 and Path 2 direct towards a scanning mirror and a fixed mirror, respectively.[84] Subsequently, the two beams are reflected off these mirrors and back to interact with the sample, and ultimately, these signals are recorded by a detector.[84] In this process, there are two cases happened. In the case of no distance difference between Path 1 and Path 2, constructive interference will be created, and a strong signal will be detected.[84] On the contrary if the infrared radiation is out of phase, there will be no signal detected.[84]

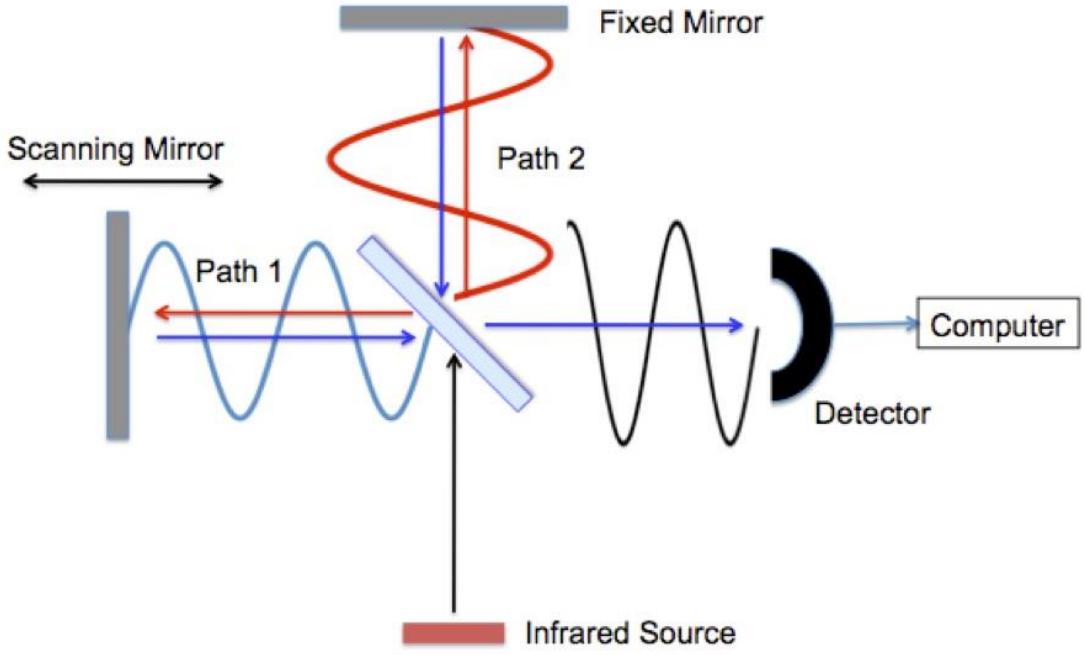

Figure 21 A schematic of an interferometer in a Fourier transform infrared spectrometer[84]

In this study, FTIR spectra were collected in the wavenumber range from 400 cm^{-1} to 4000 cm^{-1} with a repetition of 20 scans on a Bruker Optics Vertex 70 Spectrometer.

2.1.4 X-Ray Photoelectron Spectroscopy (XPS)

X-ray photoelectron spectroscopy (XPS) is a surface-sensitive and quantitative technique that measures the elemental composition, electronic state, and chemical state of the surface of a material.[85] XPS is an ultra-high vacuum-based measurement and it can typically detect to a depth of 10 nm.[85]

Figure 22 (a) illustrates the basic components of XPS instrument including the X-ray source, electron energy analyzer, electron collection lens, sample holder, and electron detector.[86] As shown in Figure 22 (b), XPS works on the principle when the sample is

exposed to X-ray radiation, electrons at the surface of atoms are ejected from the surface of the sample due to the gained energy from X-rays, which is sufficient for electrons to surmount the binding energy of the nucleus, and the leftover energy is converted into kinetic energy.[87] The elements present in the sample can be identified in light of the kinetic and binding energies which can be collected by the detector. Moreover, the intensity of these ejected electrons (also called photoelectrons) can tell information about the concentration of each element existing at the surface of the sample.[85] The relationship between kinetic energy, kE, and binding energy, BE, can be expressed as:

$$kE = \mathrm{h}v - BE - \Phi_s$$

where h is Planck's constant, v is the frequency of X-rays, and Φ_s is the work function for the specific surface of the sample.[86]

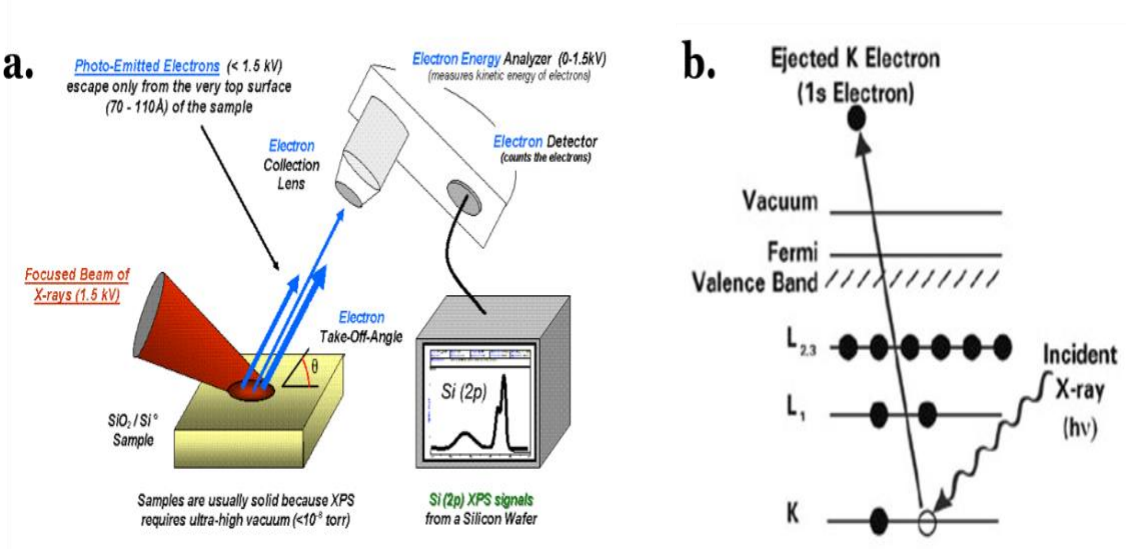

Figure 22 (a) A schematic of X-ray photoelectron spectrometer; (b) The diagram of XPS working principle[86,87]

In this work, XPS measurement was performed with a Thermo-VG Scientific ESCALab 250 microprobes. The spectra were recorded with a beam of 200 μm diameter at 1486.6 eV and 49.3 W. All of reported binding energies were normalized against the binding energy of C 1s peak at 284.8 eV. Survey spectra with binding energy from 0 to 1200 eV were collected for each sample to determine the relative composition of elements at the surface of the sample. The XPS results were analyzed by utilizing the software named CasaXPS, and the background types including U 2 tougaard and Shirley were chosen for peak deconvolution and fitting.

2.2 Electrochemical Characterization Techniques

In this section, the electrochemical characterization techniques will be presented, containing cyclic voltammetry (CV), battery capacity test, battery cyclability, and rate capability test.

2.2.1 Cyclic Voltammetry (CV)

The cyclic voltammetry (CV) is a very powerful electroanalytical technique to study the oxidation and reduction processes of molecules.[88] It is also a valuable approach to investigate the redox potential, electrochemical reaction rate, and electron transfer in chemical reactions.[89] The cyclic voltammetry potential waveform is shown in Figure 23, the CV performs a linear potential sweep to the working electrode at a steady scan rate, from the negative potential to the positive potential first (t_0-t_1) and then in the opposite direction (t_1-t_2).[89]

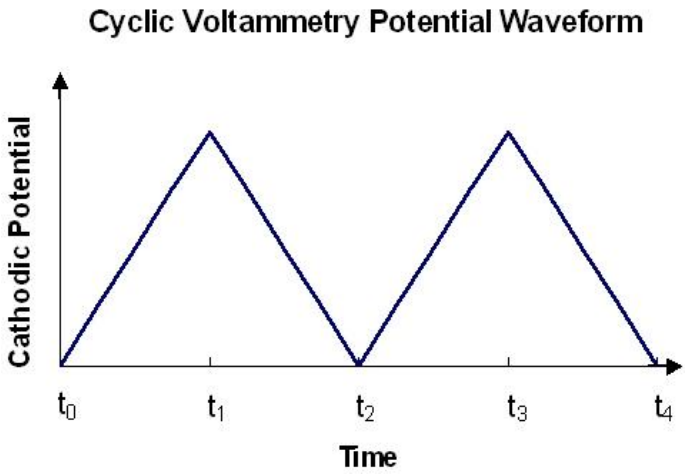

Figure 23 The cyclic voltammetry potential waveform [90]

Moreover, a typical voltammogram is illustrated in Figure 24. The x-axis represents the scanned potential, and the y-axis refers to the current. When the scanned potential increases, the current starts to increase as well, resulting in an anodic (also called oxidative) potential peak (E_{pa}), and the peak value is the anodic current (i_{pa}).[89] Because the electrons flow from the electrolyte to the electrode surface, there is a current formed during this process. Afterwards, the current starts to decrease until the scanned potential reaches its maximum value. In the reverse cycle, the applied scanned potential sweeps in the negative direction, and the measured current becomes increasingly negative until it reaches the anodic peak.[89] The peak cathodic (also known as reductive) potential (E_{pc}) and cathodic current (i_{pc}) can be obtained as well.[89]

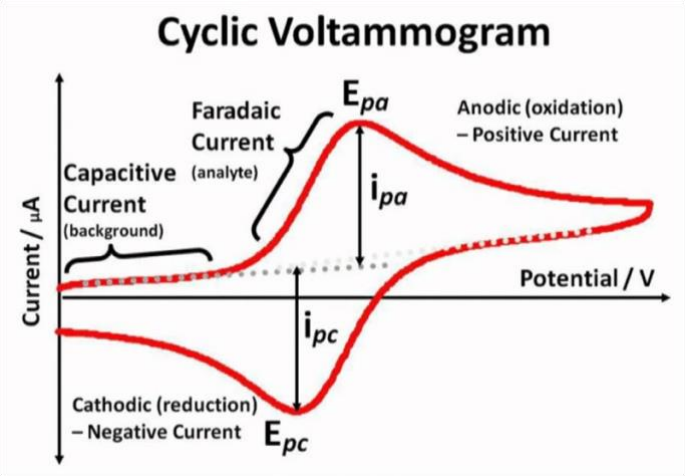

Figure 24 A typical cyclic voltammogram[91]

In this work, CV was used to detect the reduction and oxidation potentials of the metal ions inside the coin batteries. The Bio-Logic VMP3 potentiostat was used for the CV measurement at 0.1 mV/s scan rate in a voltage range of 1.0 V - 2.0 V with polished zinc foil as the counter and reference electrode. The electrolyte is 2M $ZnSO_4$ + 0.2M $MnSO_4$ with an adjusted pH of 4.0 $\pm$ 0.2.

2.2.2 Battery Capacity Test

The battery capacity test was performed with the NEWARE BTS4000-5V battery tester, which is shown in Figure 25. The battery capacity was measured at a constant current mode between 1.0 V and 1.9 V with a current density of 50 mA/g. To begin with, the well assembled coin cells were first discharged to 1.0 V, and then recharged back to 1.9 V. That is a full discharge/charge cycle, and the coin cells were tested for first 50 cycles.

Figure 25 An image of the NEWARE BTS4000-5V battery tester[92]

2.2.3 Battery Cyclability Test

The battery cyclability test was performed with the same NEWARE BTS4000-5V battery tester. The coin cells with the same structure and components were tested between 1.0 V and 1.9 V at 50 mA/g and 500 mA/g, respectively. At a small discharging current density of 50 mA/g, the coin cells were tested for 100 cycles. At a larger discharging current density of 500 mA/g, the coin cells were tested for 1000 cycles. The capacity retention can be calculated using the following equation:

$$capacity\ retention = \frac{specific\ discharge\ capacity\ of\ the\ x\ cycle}{the\ highest\ specific\ discharge\ capacity} \times 100\%$$

The above equation can be applied in calculating the battery's capacity retention at the *x* cycle. Generally, the highest specific discharge capacity is from the first cycle, but it varies with different kinds of batteries and testing conditions.

2.2.4 Battery Rate Capability Test

The battery rate capability test was performed with the same instrument shown in Figure 25 above. Different coin cells were tested at 0.05 A/g for the first 10 cycles, then they were tested for 5 cycles at each current density in the order of 0.1 A/g, 0.2 A/g, 0.5 A/g, 1 A/g, and 2 A/g. Afterwards, they were tested at 0.05 A/g again to test their reversibility and rate capability. The batteries were tested at a constant current mode with a voltage range of 1.0V to 1.9V as well.

Chapter 3: Gelatin coated self-made ε-MnO_2 as cathode material in aqueous rechargeable zinc-ion batteries

3.1 Synthesis of self-made ε-MnO_2 and preparation of gelatin solutions

Self-made ε-MnO_2 was synthesized through co-precipitation method, and the gelatin solutions were prepared by simple magnetic stirring and heating method. More details will be discussed in section 3.1.1.

3.1.1 Synthesis of self-made ε-MnO_2

The ε-MnO_2 was synthesized through an innovative, safe, easy, and cost-effective co-precipitation method.[93] 0.01 mol manganese sulfate monohydrate ($MnSO_4 \cdot H_2O$, Sigma-Aldrich, purity ≥ 99%) and 0.02 mol sodium hydroxide (NaOH, Sigma-Aldrich, purity ≥ 97%) were dissolved in 250 ml DI water and 50 ml DI water through magnetic stirring method in different beakers, respectively. After both of them have been completely dissolved and the solutions were clear, add 0.01 mol hydrogen peroxide (H_2O_2, Sigma-Aldrich, 30 wt% in H_2O) into the NaOH solution. Afterwards, slowly add the mixture of NaOH and H_2O_2 solution into the $MnSO_4$ solution, and the solution turned into black with the emission of oxygen. Then, cover the beaker with an aluminum foil and magnetic stir the solution for 24 hours. The overall chemical equation is shown below. The Mn^{2+} first reacted with OH^- to form the manganese hydroxide ($Mn(OH)_2$), then $Mn(OH)_2$ was oxidized by H_2O_2 and formed MnO_2.

$$MnSO_4 \cdot H_2O + 2NaOH + H_2O_2 = MnO_2 \downarrow + Na_2SO_4 + 3H_2O$$

After 24 hours' magnetic stirring, the solution was centrifuged and washed three times with DI water to remove the impurity, such as Na^+ and SO_4^{2-}. Afterwards, the centrifuged MnO_2 slurry was dried in an incubator at 80 °C for 24 hours to obtain the MnO_2 solid, then the MnO_2 solid was manually ground into MnO_2 powder. Next, the ground MnO_2 powder was calcined in oven at 250 °C for 6 hours to remove the crystallization water inside the MnO_2. After 6 hours calcination, let the oven and MnO_2 powder naturally cool overnight. A schematic of main procedures is shown below in Figure 26.

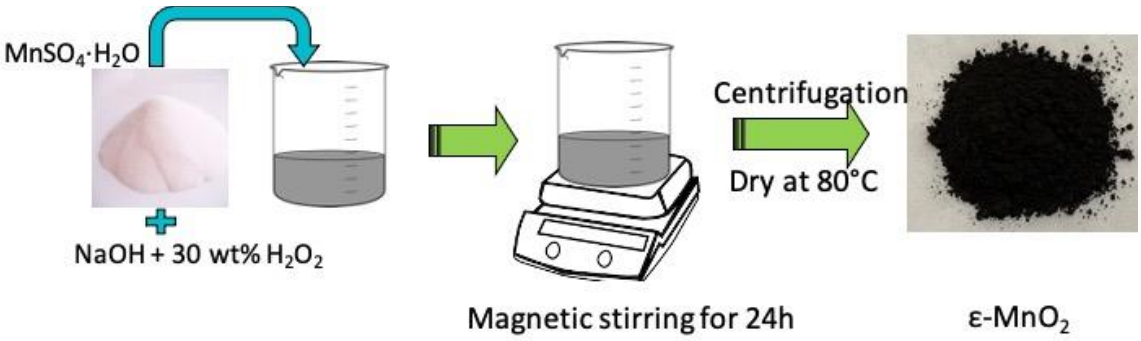

Figure 26 A schematic of main procedures to synthesize ε-MnO_2

3.1.2 Prepare gelatin solutions

The gelatin solutions were prepared by simple magnetic stirring and heating methods. 0.3 wt%, 0.5 wt%, 0.7 wt%, 1 wt%, 3 wt%, and 5 wt% gelatin solutions were prepared in 20 ml glass vials separately, and each vial contained 15 g solution. Therefore, 0.045g, 0.075g, 0.105g, 0.15g, 0.45g, and 0.75g gelatin powder (Sigma-Aldrich) were added into 14.985g, 14.955g, 14.925g, 14.985g, 14.85g, 14.55g, and 14.25g DI water, respectively. Afterwards, magnetic stirring these solutions for 12 hours at 40 °C to get the completed dissolved solutions. A picture of these prepared gelatin solutions is shown in Figure 27.

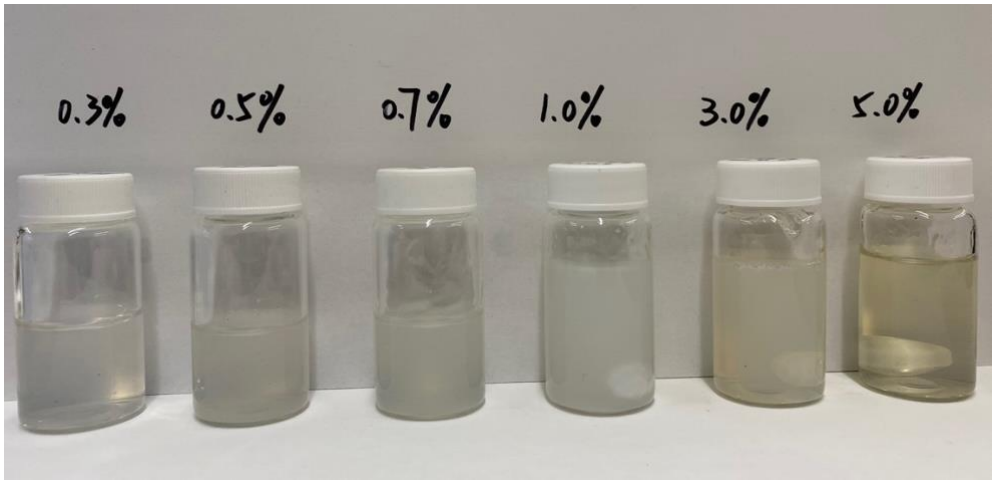

Figure 27 A picture of 0.3 wt%, 0.5 wt%, 0.7 wt%, 1 wt%, 3 wt% and 5 wt% gelatin solutions

3.2 Cathode Fabrication and Battery Assembling

After the ε-MnO_2 powder was obtained through the first step, it can be made into cathode through the following procedures. 70 wt% ε-MnO_2 (active material), 20 wt% acetylene black (conductive agent, MTI), and 10 wt% polyvinylidene fluoride (PVDF, Sigma-Aldrich) in N-methyl-2-pyrrolidone (NMP, Sigma-Aldrich, purity ≥ 99%) solution (binder) were mixed together to form a slurry. Then the slurry was uniformly coated onto a conductive polyethylene (PE) film (All-Spec 854-36150) with a mass loading of active material of 2.5 mg/cm^2. Afterwards, the film was dried at 60 ℃ for 12 hours and cooled naturally for 1 hour.

Then the dried PE film was cut into small discs with a diameter of 12 mm, which acted as the cathode in battery. The polished zinc metal foil (Rotometals, thickness: 0.2 mm) was cut into small discs with a diameter of 12 mm to act as the anode. The absorbed glass mat (AGM) separator (NSG Corporation, thickness: 0.5 mm) was also cut into 12

mm diameter discs to keep consistent with the anode and cathode. The electrolyte was prepared with 2 M $ZnSO_4$ + 0.2M $MnSO_4$ and DI water in a volumetric flask. The CR2032 coin-cell cases and its accessory spacer and coin spring were used as well. In the end, the battery was assembled according to Figure 28 below. The cathode was put on top of the bottom case with the MnO_2 surface facing up, then place the separator on top of the cathode and add 1 ml electrolyte into the separator. Next, put other battery components according to the order of anode zinc foil, spacer, cone spring and top case. Then, the battery was crimped together by the hydraulic crimping machine (MTI, MSK-100) shown in Figure 29. Therefore, the aqueous rechargeable Zn-MnO_2 battery has been successfully assembled and was ready to be tested.

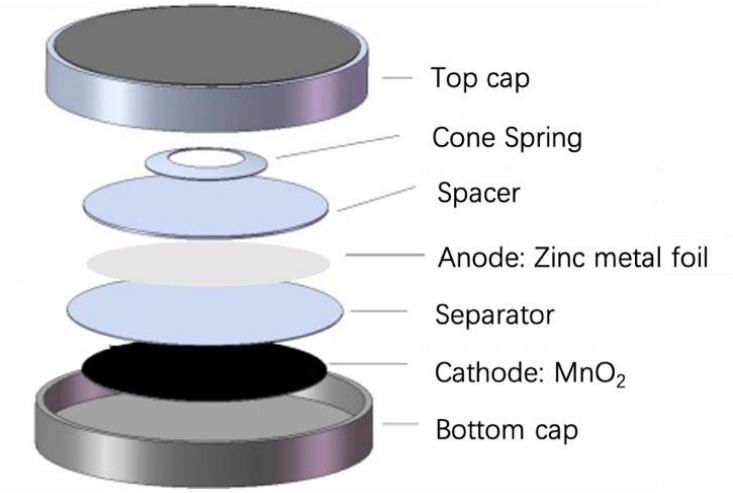

Figure 28 The basic structure of the aqueous rechargeable Zn-MnO_2 battery[94]

Figure 29 Hydraulic crimping machine (MTI, MSK-100)[95]

For the gelatin modified battery, the MnO_2 cathode surface was coated by various gelatin solutions through spin coating method by the Chemat precision spin-coater (Sigma-Aldrich, Z551562), which is shown in Figure 30. To begin with, the cathode was put in the center of the spin coater, then 1 ml gelatin solution was added on top of the MnO_2 surface, then the spin coater was operated at 2000 rpm for 60 s. Next, the cathode was dried naturally for 15 mins, and it was ready to be used in the battery assembling step with the same method of assembling unmodified Zn-MnO_2 batteries.

Figure 30 Chemat precision spin-coater (Sigma-Aldrich, Z551562)[96]

3.3 Material Characterizations

To better understand the structure and properties of the ε-MnO_2 and gelatin modified ε-MnO_2 cathode, scanning electron microscope (SEM), X-ray diffraction (XRD), Fourier transform infrared spectroscopy (FTIR), and X-ray photoelectron spectroscopy (XPS) were performed to further invstigate the material.

Scanning electron microscope (SEM) was used to better understand the morphology and topography of the material. As shown in Figure 31 below, there were two SEM images of ε-MnO_2 in 1 μm and 100 nm scale. From the 100 nm scale image, it was observed that ε-MnO_2 was nanorods with diameters of 50-100 nm. From the 1μm scale image, it showed the length of the nanorods was 1-2 μm, and the nanorods aggregated together to form a sphere. That is the morphology of the ε-MnO_2 powder.

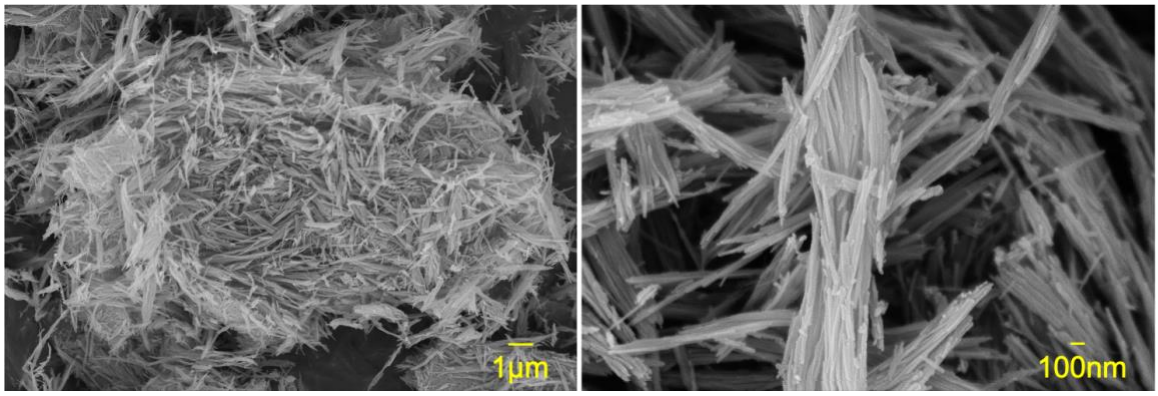

Figure 31 SEM images of ε-MnO_2 in different scales

After ε-MnO_2 was spin-coated with gelatin solutions, SEM image was also taken to understand their morphology difference before and after the gelatin coating. As shown in Figure 32 below, the gelatin molecules have been successfully coated on the ε-MnO_2 surface, and there were also some interactions between the ε-MnO_2 and gelatin, which could be further investigated using other techniques.

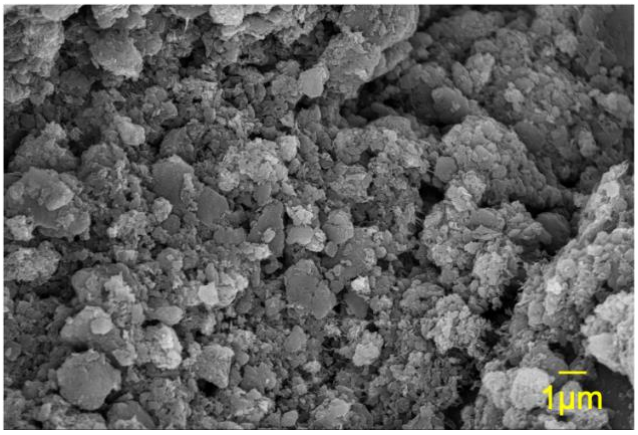

Figure 32 A SEM image of 0.5 wt% gelatin coated ε-MnO_2

X-ray diffraction (XRD) was also done to understand the crystal strcuture and properties of the MnO_2 powder because MnO_2 has various phases, including α-MnO_2, β-

MnO_2, γ-MnO_2, δ-MnO_2, λ-MnO_2 and ε-MnO_2. The result is shown below in Figure 33. According to the signal peaks and compare them with the standard cards of JCPDS No. 30-0820, it showed that the self-made MnO_2 is ε-MnO_2 with hexagonal unit cells structure of a = 0.280nm and c = 0.445nm.[97] Since the ionic radii of Zn^{2+} is 74 pm (0.074nm), the hexagonal unit cells structure allows the Zn^{2+} intercalation/ deintercalation process easily.

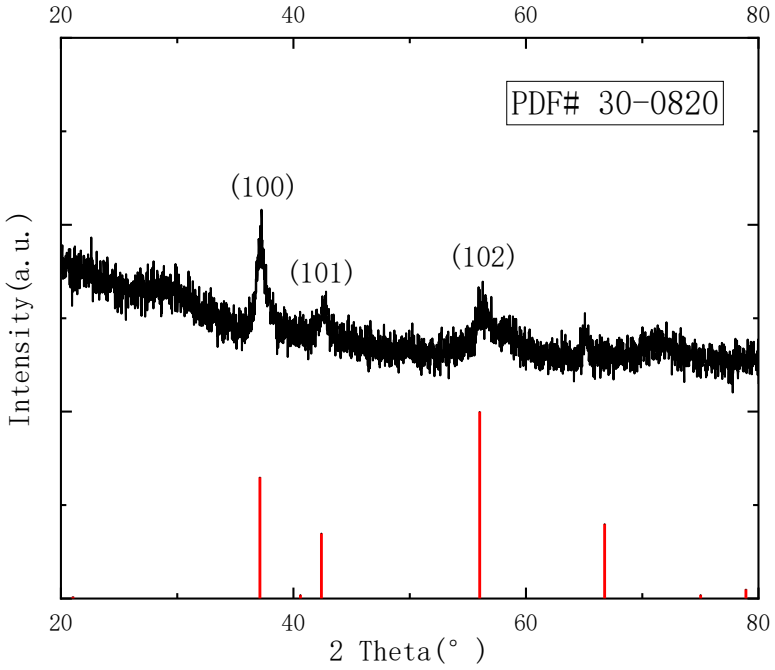

Figure 33 XRD result of self-made MnO_2 powder

Fourier transform infrared spectroscopy (FTIR) was also done to determine if the gelatin has been successfully coated on top of the ε-MnO_2 cathode. From the FTIR results in Figure 34, it could be determined that N-H bond, C-N bond and R'(C=O) NH_2 bond all existed in gelatin coated ε-MnO_2 cathode, which is a strong proof that gelatin has been successfully coated on the cathode compared to uncoated ε-MnO_2 cathode. That is because gelatin consists of amino acids, and N-H bond, C-N bond and R'(C=O) NH_2 bond are all

featured bonds of the amino acids. Therefore, it strongly proved that gelatin has been coated on the MnO_2 cathode. More interestingly, as the concentration of gelatin increasing, the corresponding transmittance decreased, which is also reasonable because the higher concentration gelatin solution has more molecules in the same 1ml solution. Therefore, gelatin molecules can reflect and absorb lighter, resulting in a lower transmittance.

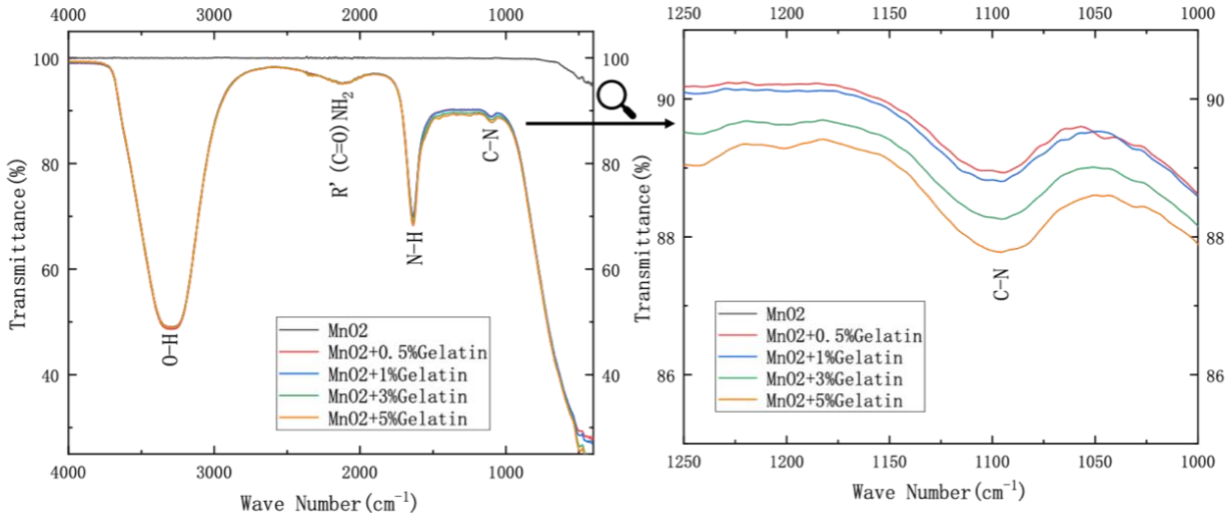

Figure 34 FTIR results of MnO_2 and gelatin coated MnO_2 cathode

X-ray photoelectron spectroscopy (XPS) was conducted to investigate the component of the ε-MnO_2 cathode and gelatin coated cathode. As shown in Figure 35 (a) and (b) below, the survey spectrum and Mn 2p spectrum of the MnO_2 cathode were done to figure out the component of the MnO_2 cathode and the oxidation state of the Mn. According to Figure 35 (a), the MnO_2 cathode was detected to have manganese (Mn), oxygen (O), carbon (C), nitrogen (N) and fluorine (F) elements. More specifically, Mn and O were from the MnO_2, C was from the acetylene black, and N and F were from the polyvinylidene fluoride

(PVDF). To better understand the oxidation state of Mn in the sample, a high-resolution scan of Mn was also performed. As shown in Figure 35 (b), the two peaks of 642 eV and 654 eV were detected, which are referred to Mn $2p_{3/2}$ and Mn $2p_{1/2}$, respectively.[98] Moreover, since the detected oxidation state of Mn was +4, it perfectly proved the oxidation state and purity of the self-made MnO_2.

The gelatin coated MnO_2 cathode was also measured using XPS to determine the existence of gelatin. The survey spectrum and N 1s spectrum of 0.5 wt% gelatin coated MnO_2 cathode were shown in Figure 35 (c) and (d). Compare the survey spectrum of 0.5 wt% gelatin coated MnO_2 cathode with the survey spectrum of uncoated MnO_2 cathode, it was clearly shown that the nitrogen percentage has significantly increased. That is very reasonable because the addition of gelatin dramatically increased the nitrogen percentage in the sample. Furthermore, the N 1s spectrum of gelatin coated MnO_2 cathode has also been done to prove the successful coating of gelatin shown in Figure 35 (d). The peak at 400 eV perfectly matched C-NH_2 bond,[99] which also strongly proved the existence of gelatin. Therefore, these XPS spectra clearly proved that the self-made MnO_2 is made of Mn^{4+} and there is no Mn^{3+} impurity, and the gelatin has been successfully coated on the MnO_2 surface as well.

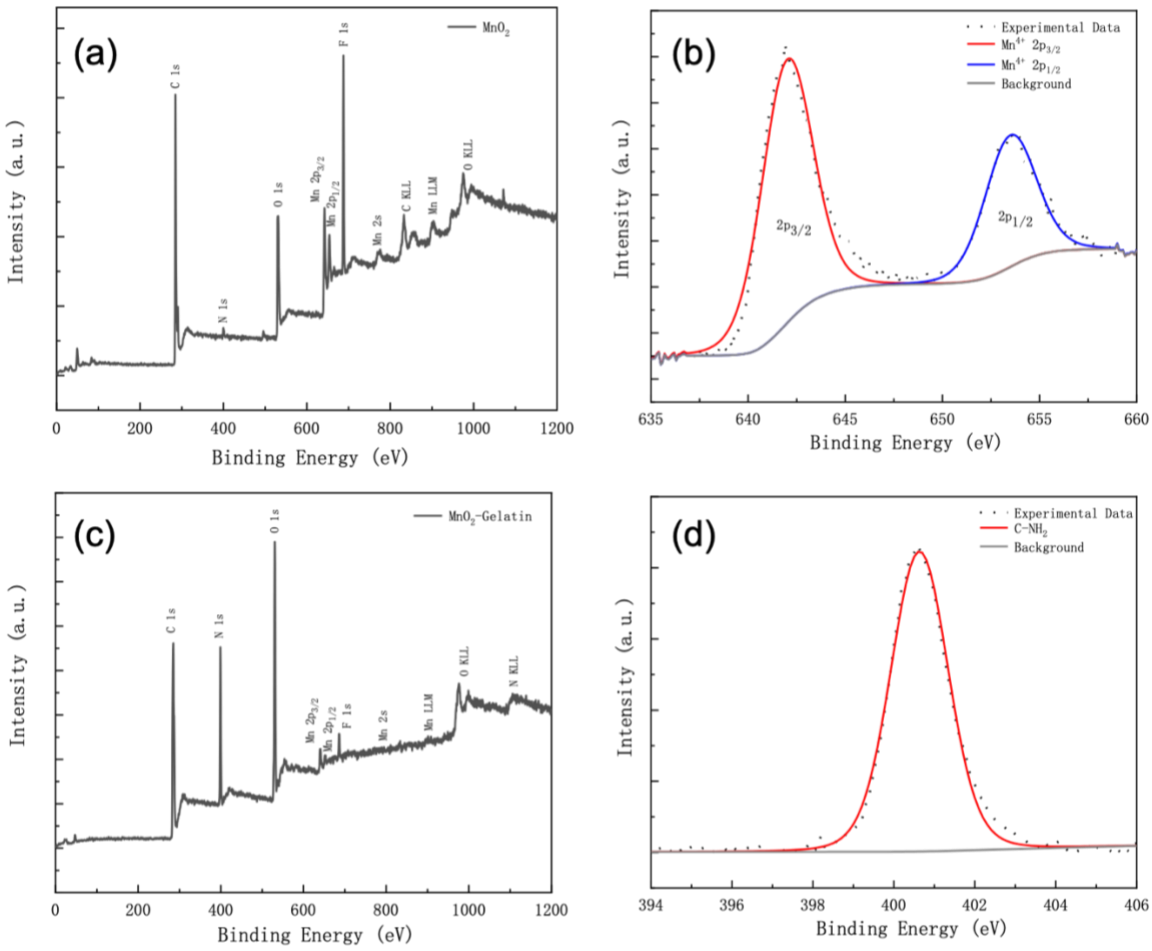

Figure 35 XPS spectra of (a) survey spectrum and (b) Mn 2p spectrum of MnO_2 cathode; (c) survey spectrum and (d) N 1s spectrum of 0.5 wt% gelatin coated MnO_2 cathode

3.4 Electrochemical Characterizations

Electrochemical characterizations have also been done to determine the battery performance variation before and after gelatin coating. Cyclic voltammetry (CV) test, battery capacity measurement, cycling and rate performance measurement were done to investigate the battery electrochemical properties and the influence of gelatin coating.

Cyclic voltammetry (CV) tests were conducted to figure out the reaction voltage and mechanism. As shown in Figure 36 (a) and (b), they are CV tests for the Zn-MnO_2 battery without gelatin coating at 0.1 mV/s. During the 1st discharge/charge cycle, the redox peaks were at 1.24 V and 1.55 V, which was corresponding to the Zn intercalation /deintercalation process. Then during the 2nd and 3rd cycles, it appeared two pairs of redox peaks at 1.29 V/1.55 V and 1.38 V/1.59 V, indicating a two stepwise intercalation of Zn^{2+} ions.[31] Afterwards, the CV tests were carried out on Zn-MnO_2 battery with 0.5 wt% gelatin coated cathode, and the results are shown in Figure 36 (c) and (d). During the 1st discharge and charge cycle, the redox peaks shifted to 1.17 V/1.67 V, which might be due to the interaction between the gelatin and MnO_2 though hydrogen bonds and van der Waal's force. More specifically, these interactions would stint the movement of Zn^{2+} and Mn^{2+}, and it required a stronger drifting power to overcome these forces for intercalation and deintercalation, resulting in a larger voltage difference and redox peaks shift in the end.

Moreover, during the 2nd and 3rd cycles in Figure 36 (d), there was also a two stepwise intercalation of Zn^{2+} ions during the reduction process, which was the same situation as the battery with unmodified cathode. However, the peaks shifted again to 1.22 V and 1.33 V/1.65 V, which could be explained as the interaction between the gelatin and MnO_2 as well. Another interesting finding was that the peak width also increased after gelatin coating. The peak width represented for the reaction speed, and the sharper the peak was, the faster the reaction speed was.[88] Therefore, this indicated

that the gelatin coating reduced the reaction rate, which was also a strong evidence of the interaction between gelatin and Zn^{2+} and Mn^{2+} ions.

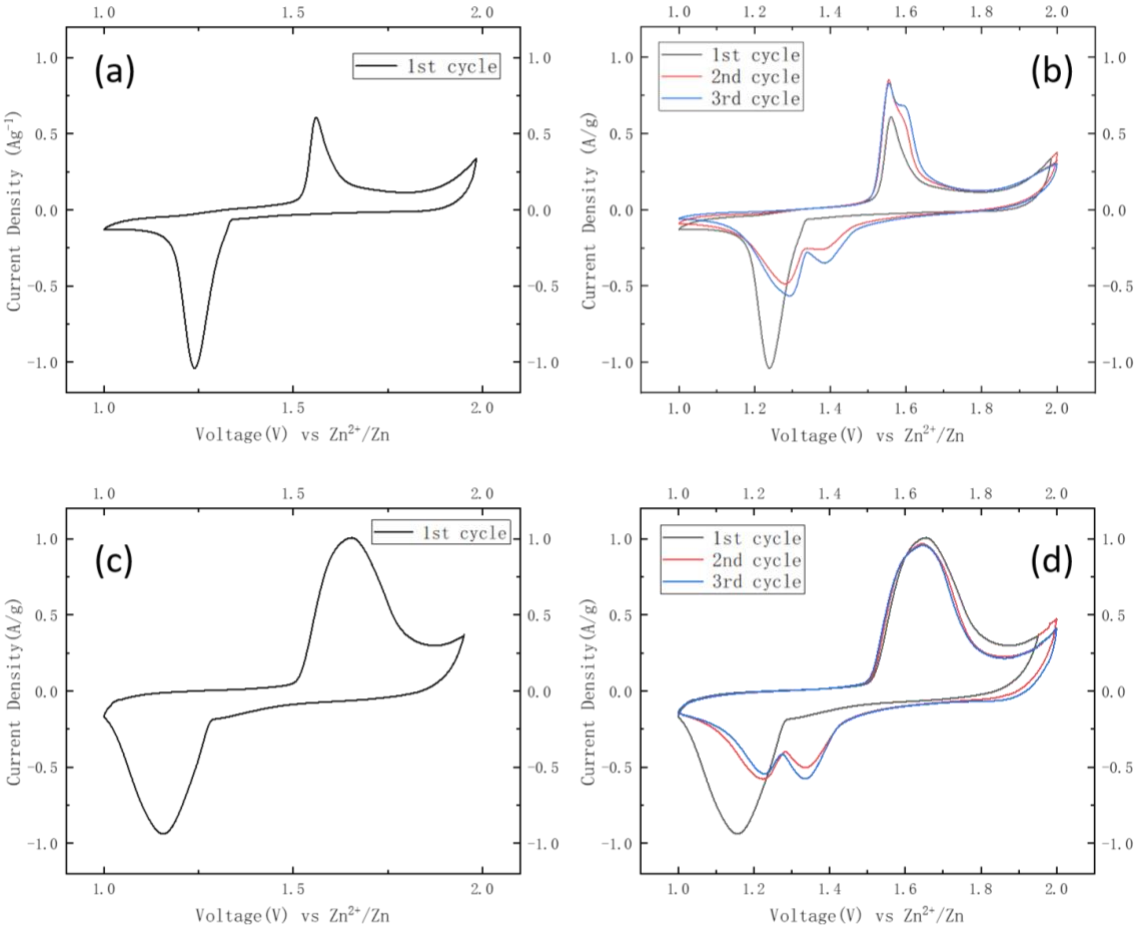

Figure 36 The cyclic voltammograms of (a) 1st cycle and (b) 1-3 cycles of Zn-MnO_2 battery with unmodified cathode, and (c) 1st cycle and (d) 1-3 cycles of Zn-MnO_2 battery with 0.5 wt% gelatin coated cathode

The battery capacity tests were done as well to evaluate the batteries' electrochemical performance. As shown in Figure 37, the unmodified Zn-MnO_2 battery exhibited a high specific discharge capacity of 330 mAh/g at 50 mA/g, and the gelatin modified Zn-MnO_2

battery showed a similar discharge capacity of 330 mAh/g at 50 mA/g. These results suggested that the gelatin coating did not influence the discharge capacity of the battery. More interestingly, there were also two platforms during each discharge and charge process, which was consistent with the CV test results. For instance, in the left graph of Figure 37, the two platforms were at 1.50 V and 1.57 V during the charging process, and another two platforms were located at 1.30 V and 1.40 V during the discharging process. These results were consistent with the CV results, which was also a proof for the two stepwise Zn^{2+} intercalation process.

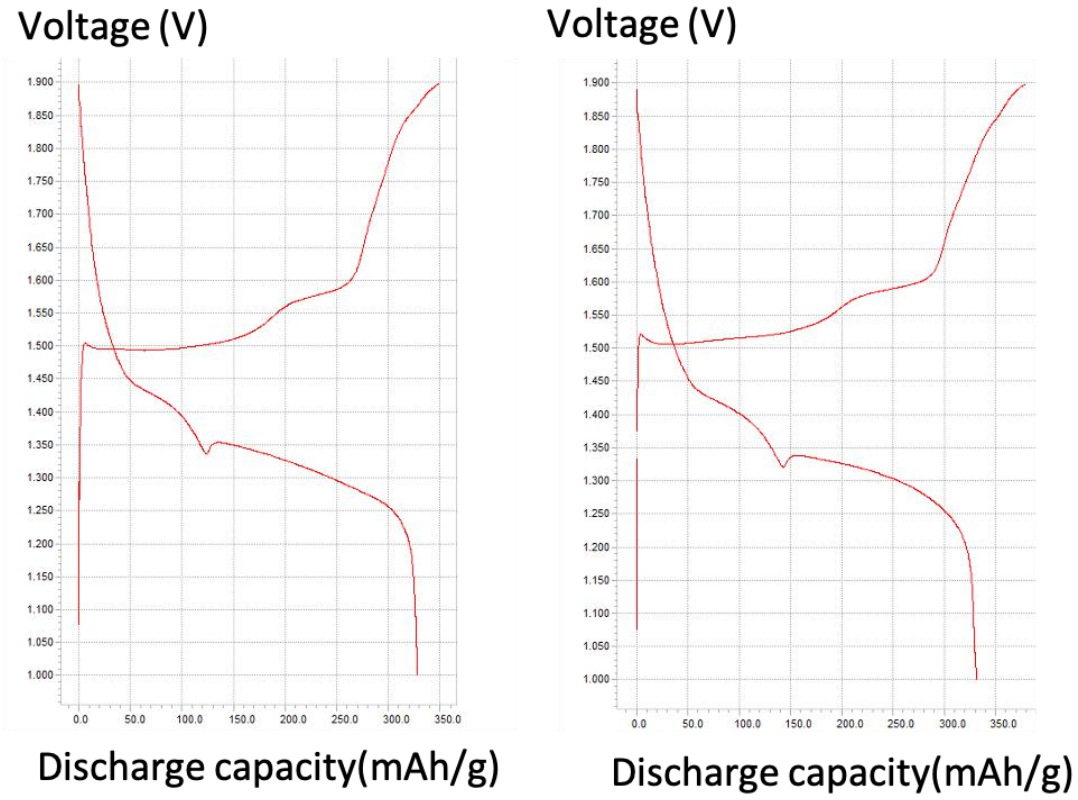

Figure 37 The battery capacity tests for an unmodified Zn-MnO_2 battery (left) and a Zn-MnO_2 battery with gelatin coated cathode (right)

The battery cycling performance was investigated using the NEWARE BTS4000-5V battery tester to measure its cyclability at different charging rate. The cycling performance results of unmodified Zn-MnO_2 battery are shown in Figure 38 (a) and (b) below. At 50 mA/g charging rate, the battery exhibited a high specific discharging capacity of nearly 400 mAh/g, but it could only keep 80% capacity retention for about 20 cycles, which was not a satisfying cyclability. At a high current density of 500 mA/g, the battery displayed a discharging capacity of 150-175 mAh/g, and the capacity kept 80% for approximately 200 cycles. Therefore, the unmodified Zn-MnO_2 battery showed a better cycling performance at larger charging rate of 500mA/g.

The cycling performance of Zn-MnO_2 battery with gelatin coating has also been measured at 50 mA/g and 500mA/g, respectively. As shown in Figure 38 (c), the gelatin coated cathode showed a high discharging capacity of nearly 400 mAh/g at 50 mA/g, and the capacity can keep 80% for 35 cycles, which has been improved by 75% compared with the unmodified battery. Moreover, at the larger charging rate of 500mA/g shown in Figure 38 (d), the battery showed a capacity of 100-125 mAh/g, and the battery could keep 80% capacity for 1000 cycles, which was a dramatical improvement of 400% in cyclability compared with unmodified Zn-MnO_2 battery. Although there was some capacity lost at 500mA/g, it was negligible compared with the significant enhancement in cycling performance. Furthermore, the cycling curve of the gelatin coated cathode was more stable compared with the unmodified one. For the unmodified battery cycling test, there was a slight capacity increase in the first 20 cycles, which can be explained by the deposition of Mn^{2+} in electrolyte onto the MnO_2 cathode because it also contributed to the capacity and

resulted in a slight capacity increase. However, with the gelatin coating on top of the MnO_2 cathode, the Mn^{2+} could not easily enter or escape in/from the MnO_2 because gelatin could confine the Mn^{2+} through hydrogen bonds and van der Waal's force.[31] Therefore, the battery with gelatin coating has a better cycling performance compared with the unmodified Zn-MnO_2 battery.

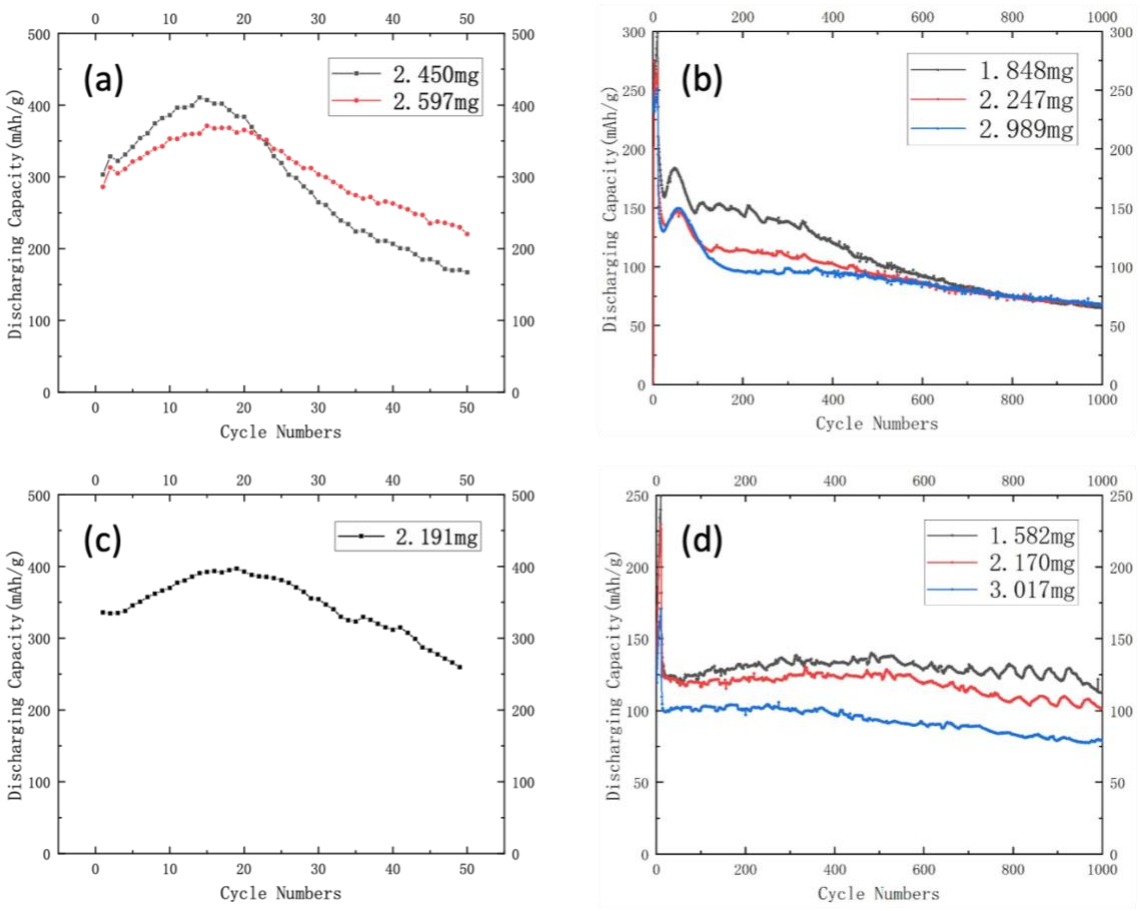

Figure 38 The battery cycling performance of unmodified Zn-MnO_2 battery at (a) 50 mA/g and (b) 500 mA/g, and the cycling performance of gelatin coated Zn-MnO_2 battery at (c) 50 mA/g and (d) 500 mA/g

The rate performances of the batteries with the unmodified and gelatin coated cathode were also measured at 0.05 A/g, 0.1 A/g, 0.2 A/g, 0.5 A/g, 1 A/g and 2 A/g to investigate the electrochemical performance of the batteries. As shown in Figure 39, the left graph is the rate performance test for unmodified Zn-MnO_2 battery. It exhibited an average discharging capacity of 330 mAh/g at 0.05 A/g for first 10 cycles. Afterwards, as the current density increased, the battery capacity decreased accordingly. The battery capacity was about 300 mAh/g, 250 mAh/g, 150 mAh/g, 75 mAh/g and 50 mAh/g at 0.1 A/g, 0.2 A/g, 0.5 A/g, 1 A/g and 2 A/g, respectively. Since the depth of discharge of the higher discharging rate was smaller than the lower discharging rate, the cathode and anode material might not fully participate in the redox reaction at higher discharging rate, which resulted in a capacity reduce in the end.[100] Then, the battery was tested at 50 mA/g again to investigate its reversibility, and the battery capacity could still reach 330 mAh/g at 50 mA/g but with a strong decreasing tendency, which is not a very desirable rate performance.

For the gelatin coated cathode, its discharge capacity could reach 225 mAh/g at 50 mA/g at the beginning, then the capacity decreased with the increasing discharging rate as well. The capacity was about 130 mAh/g, 115 mAh/g, 75 mAh/g, 55 mAh/g and 50 mAh/g at 0.1 A/g, 0.2 A/g, 0.5 A/g, 1 A/g and 2 A/g discharging rate, respectively. The discharge capacity of gelatin modified cathode decreased compared to the unmodified battery, which could be interpreted by the interactions between the gelatin and MnO_2. Because at a higher discharging rate, the battery capacity decreased originally, and with the addition of gelatin on MnO_2, the reaction rate could be further reduced according to the CV results. Therefore, at a higher discharging rate, the capacity of gelatin coated cathode capacity would be

influenced accordingly. However, the gelatin coated cathode showed a more stable discharging performance at different current densities compared to unmodified battery, which is also a strong proof for its excellent cycling performance.

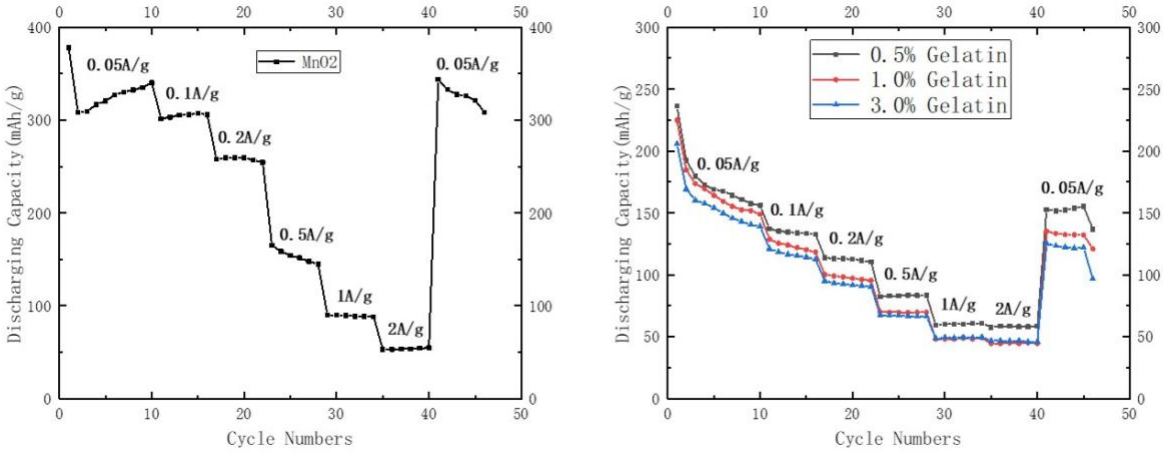

Figure 39 The rate performance of the unmodified Zn-MnO_2 battery (left) and the gelatin coated Zn-MnO_2 battery (right) at 0.05 A/g, 0.1 A/g, 0.2 A/g, 0.5 A/g, 1 A/g and 2 A/g

3.5 Conclusions

In conclusion, the self-made ε-MnO_2 cathode material has been successfully synthesized through co-precipitation method. The gelatin solutions with different concentration have also been prepared and coated on top of the ε-MnO_2 cathode by spin coating method. Then, the unmodified and gelatin coated Zn-MnO_2 batteries have been well assembled into coin cells and tested.

The self-made ε-MnO_2 cathode material and gelatin coated ε-MnO_2 cathode were characterized by SEM, XRD, FTIR and XPS. The SEM images showed the morphology of the ε-MnO_2 was nanorods with the diameters of 50-100 nm and length of 1-2 μm. The

XRD result indicated that the crystal structure of the self-made ε-MnO_2 is hexagonal unit cells structure with a = 0.280nm, c = 0.445nm. The FTIR results demonstrated that gealtin has been succssfully coated on the ε-MnO_2 cathode because the featured bonds of N-H bond, C-N bond and R'(C=O) NH_2 bond in gelatin have been clearly detected. The XPS results also proved that the gelatin has been coated on the ε-MnO_2 cathode since the C-NH_2 bonds was found in the N 1s spectrum of the gelatin coated ε-MnO_2. These characterizations together illustrated the structure and properties of ε-MnO_2 and proved the successfully coating of gelatin on ε-MnO_2.

The electrochemical characterizations have also been done to investigate the electrochemical performance of the unmodified and gelatin coated Zn-MnO_2 batteries, including CV tests, battery capacity measurement, cycling and rate performance. The CV tests showed that the gelatin modified battery has higher oxidation potential, suggesting the interactions between the gelatin and MnO_2 cathode. Moreover, two kinds of batteries both exhibited excellent specific discharge capacity of 350 mAh/g and good rate performance. More importantly, the gelatin coated battery showed a distinguished cyclability of 1000 cycles with 80% capacity retention at 500 mA/g, which is 400% higher than the unmodified battery.

Therefore, the gelatin coating could significantly increase the cycling performance of aqueous rechargeable Zn-MnO_2 battery to 1000 cycles, and it also opens a pathway for other researchers to further improve the Zn-MnO_2 battery performance. This kind of high energy density, high cyclability, high safety, cost effective and environmentally friendly battery will have more potential applications in the future.

Chapter 4: PEDOT: PSS coated self-made ε-MnO_2 as cathode material in aqueous rechargeable zinc-ion batteries

4.1 Preparation of PEDOT: PSS solutions

The synthesis method of self-made ε-MnO_2 has been introduced in section 3.1, and the process of how to prepare PEDOT: PSS solutions will be introduced in this section. The PEDOT: PSS solutions were prepared using the method reported by Thomas et al. in 2020.[74] To begin with, 50 wt% of ethylene glycol (EG, Sigma-Aldrich, purity ≥ 99%) and 50 wt % of methanol (MeOH, Sigma-Aldrich, purity ≥ 99.9%) were mixed together to form the EM solution, and it acted as the solvent of PEDOT: PSS solutions. Then add 10 wt%, 16 wt%, and 20 wt% of the EM solution into the PEDOT: PSS (Sigma-Aldrich, 1.3 wt% dispersion in H_2O) to make EM-10, EM-16, and EM-20 solutions, respectively. Afterwards, these solutions were magnetically stirred for 1 hour to be blended completely together. The prepared solutions are shown below in Figure 40.

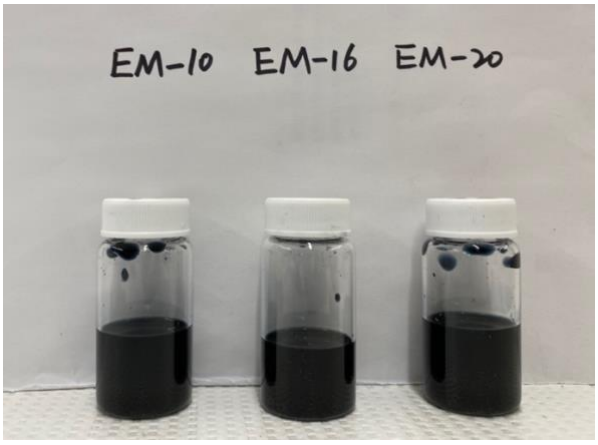

Figure 40 A picture of the prepared EM-10, EM-16 and EM-20 solutions

4.2 Cathode Fabrication and Battery Assembling

The PEDOT: PSS coated MnO_2 cathode was prepared using spin coating method as well. 1 ml of EM-16 solution was added on top of the MnO_2 cathode, then the cathode was spin coated at 2000 rpm for 60s and dried at 90 °C on a hot plate for 60s. Afterwards, the coated MnO_2 cathode was cooled naturally for 10 mins. Then, the PEDOT: PSS coated cathode is ready for the battery assembling. The battery assembling process is the same as the method mentioned in section 3.2.

4.3 Material Characterizations

In this section, scanning electron microscope (SEM), Fourier transform infrared spectroscopy (FTIR), and X-ray photoelectron spectroscopy (XPS) were performed to investigate the existence of PEDOT: PSS coating and structure of PEDOT: PSS coated MnO_2 cathode.

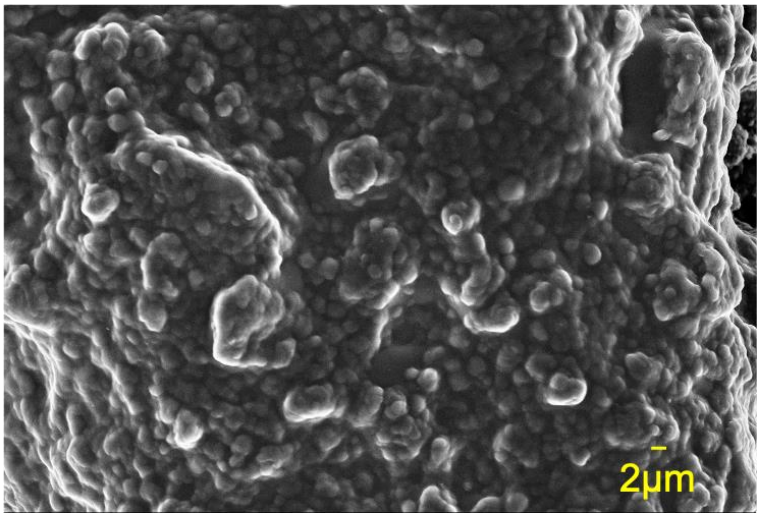

Figure 41 A SEM image of the PEDOT: PSS coated MnO_2 cathode

Scanning electron microscope (SEM) was done to explore the morphology of the PEDOT: PSS coated MnO_2 cathode. As shown in Figure 41 above, the PEDOT: PSS solution has been successfully and uniformly coated on top of the MnO_2 cathode. Compare with the unmodified MnO_2 cathode, there is almost no bare MnO_2 directly exposed. Instead, there is a uniform PEDOT: PSS layer on top of the MnO_2 sphere.

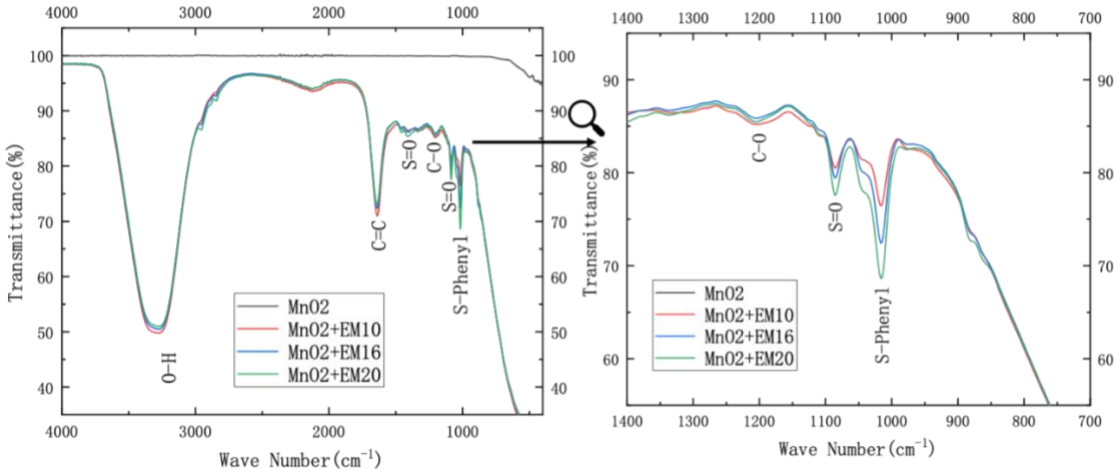

Figure 42 FTIR results of PEDOT: PSS coated MnO_2 cathode

Fourier transform infrared spectroscopy (FTIR) was tested to figure out if the PEDOT: PSS layer has been coated on top of the MnO_2 cathode. The FTIR results were displayed in Figure 42. On the left graph, it was a FTIR transmittance measurement within the wavelength of 400 – 4000 cm^{-1}. It was clearly shown that there were some peaks at 3340 cm^{-1}, 1638 cm^{-1}, 1410 cm^{-1}, 1205 cm^{-1}, 1086 cm^{-1}, and 1015 cm^{-1}, which were corresponding to O-H bond, C=C bond, S=O bond, C-O bond, and S-Phenyl bond,[101] respectively. These bonds are all featured bonds of PEDOT: PSS according to its structure,[72] which indicated the existence of PEDOT: PSS. More interestingly, the

transmittance decreased with the increasing concentration of PEDOT: PSS, which was reasonable because more molecules in the same volume solution can reflect or absorb more infrared rays, resulting in a lower transmittance value. Therefore, these FTIR resluts strongly proved the successfully coating of PEDOT: PSS on MnO_2 cathode.

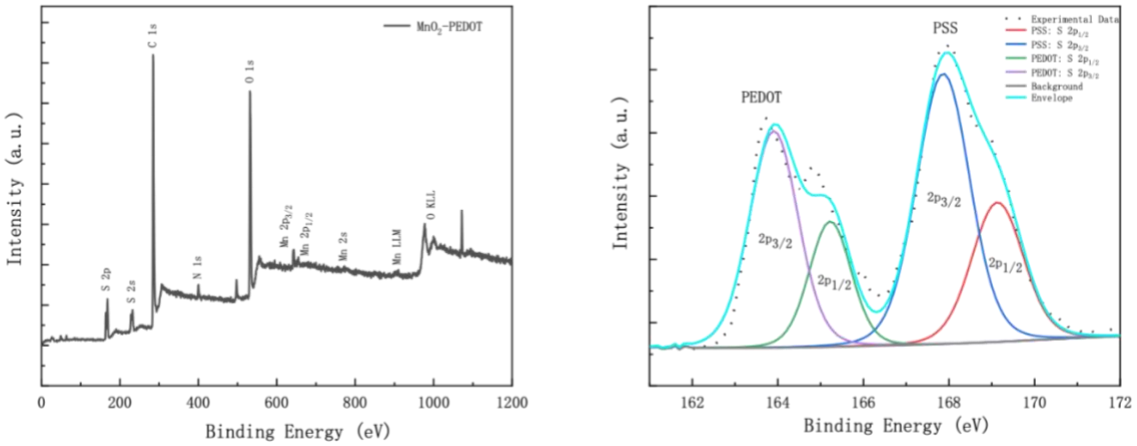

Figure 43 XPS spectra of the survey spectrum (left) and S 2p spectrum (right) of the PEDOT: PSS coated MnO_2 cathode

X-ray photoelectron spectroscopy (XPS) was conducted to prove the existence of PEDOT: PSS coating as well. As shown in Figure 43 above, they were the XPS spectra of the survey spectrum (left) and S 2p spectrum (right) of the PEDOT: PSS coated MnO_2 cathode. From the survey spectrum, it showed two standard peaks of the sulfur (S) 2p and S 2s at 168.3 eV and 227 eV, respectively, which could not be found in the uncoated or gelatin coated MnO_2 cathode. Moreover, the binding energy of these two peaks in survey spectrum was also consistent with previous study,[102,103] which strongly proved the existence of PEDOT: PSS on the MnO_2 cathode. Furthermore, from the deconvoluted high-resolution S 2p spectrum in Figure 32 (right), the featured peaks of PEDOT and PSS were

exhibited clearly, which were located at 164 eV and 168 eV separately. According to the literatures, the XPS peaks between 162 and 166 eV were designated as the S 2p band of the sulfur atom in the PEDOT, and the XPS band with a binding energy between 166 and 172 eV was designated as the S 2p band of the sulfur atom in the PSS.[104,105] Therefore, it can well explain that two groups of peaks located at 164 eV and 168 eV were from sulfur in the PEDOT and PSS, respectively. Hence, these XPS results strongly proved the successfully coating of PEDOT: PSS on top of the MnO_2 cathode.

To sum up, these material charterazation methods together demostrated the strucutre of the PEDOT: PSS coating and confirmed the successfully coating of PEDOT: PSS on the MnO_2 cathode.

4.4 Electrochemical Characterizations

Electrochemical characterizations were also performed to measure the electrochemical performance of the battery with PEDOT: PSS coated MnO_2 cathode, including Cyclic voltammetry (CV) test, battery capacity test, cycling and rate performance measurement.

Cyclic voltammetry (CV) tests were done to figure out the raction voltage and mechnism of the battery with PEDOT: PSS coated MnO_2 cathode, and to compare it with the unmodified battery to see the effect and funtion of the PEDOT: PSS coating. During the 1st discharg/charge cycle, the redox peaks appeared at 1.19 V/1.56 V. Compared with the redox peaks of umodified battery at 1.24 V/ 1.55V shown in Figure 36 (a), the redox potential of the PEDOT: PSS coated battery reduced during reduction process, which could be explained by the interactions between the PEDOT: PSS and Zn^{2+}. To be more specific,

since the PSS part carries a negative charge due to the deprotonated sulfonyl group,[68] it can attract postive metal ions, such as Zn^{2+} and Mn^{2+}. Therefore, during the reduction process, the battery requires a lager potential differnece to overcome the attacting force between Zn^{2+} and the sulfonyl group, resluting in a lower potential during the reduction process.

During the 2nd and 3rd cycles shown in Figure 44 (right), the redox peaks shifted to 1.25 V/1.55 V and 1.37 V/1.58V, which can be referred to the two stepwise intercalation/ deintercalation of Zn^{2+} ions into the MnO_2. Compared with the peaks of the unmodified battery at 1.29 V/1.55 V and 1.38 V/1.59 V shown in Figure 36 (b), there is still slight peak shifting in the reduction process, which could also be attributed to ionic interactions between the PEDOT: PSS and zinc ions.

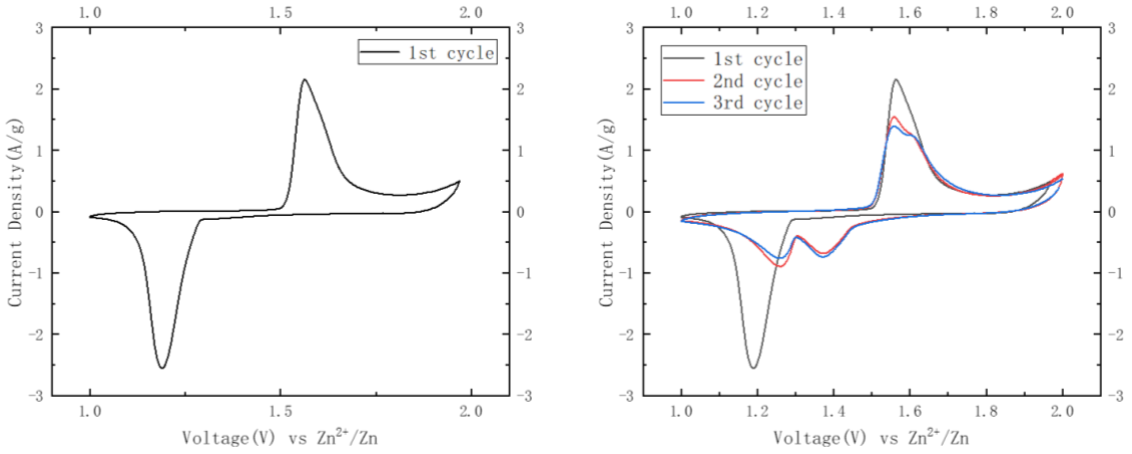

Figure 44 The cyclic voltammograms of 1st cycle (left) and 1-3 cycles (right) of Zn-MnO_2 battery with PEDOT: PSS coated MnO_2 cathode

The battery capacity test was carried out to measure the discharging capacity of the Zn-MnO_2 battery with PEDOT: PSS coated MnO_2 cathode. As shown in Figure 45, the

specific discharging capacity of the PEDOT: PSS (EM-16 solution) coated cathode was 270 mAh/g at 50 mA/g. Compared with the capacity of the unmodified Zn-MnO_2 battery of 330 mAh/g, it slightly decresed after PEDOT: PSS coating. That might be due to the uniformly coating shown in the the SEM image of Figure 41. Since the PEDOT: PSS coating is too uniform, and the MnO_2 has been almost perfectly covered, the MnO_2 cathode material might not be able to fully paticiapte in the reaction. Consequently, it caused slightly capacity decrease in the end.

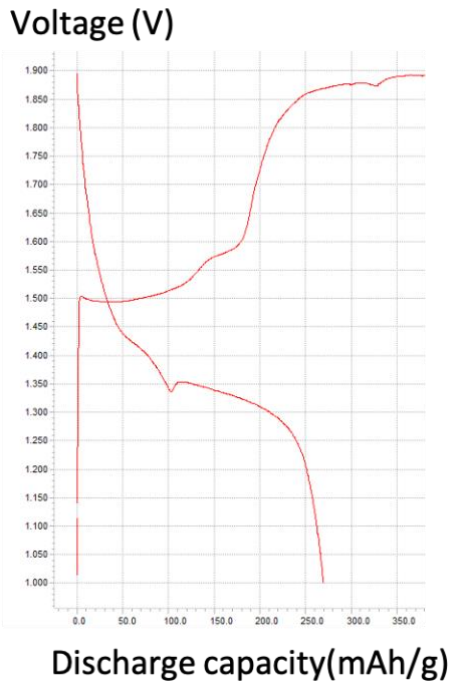

Figure 45 The battery capacity tests of a Zn-MnO_2 battery with PEDOT: PSS coated MnO_2 cathode

The battery cycling performance was tested to measure the cyclability of the the Zn-MnO_2 battery with PEDOT: PSS coated cathode. As shown in Figure 46, the PEDOT: PSS coated cathode was tested at 50 mA/g and 500 mA/g seperately. At 50 mA/g, the battery

exhibited a specific discharge capacity of 140-175 mAh/g for more than 50 cycles, which is a dramatically improvement of 150% compared with the unmodified Zn-MnO_2 battery of 20 cycles. At 500 mA/g, the battery showed a discharge capacity of 140 mAh/g, and the capcity can keep 80% for 250 cycles, which is a 25% improvement compared with the unmodified battery. Therefore, the PEDOT: PSS coated cathode presented an excellent cyclability at 50 mA/g than both of the unmodifed and gelatin coated cathodes. The mechnism could be explained by the ionic interaction of sulfonyl group and Mn^{2+}. More specifically, since the PSS part carries a negative charge due to the deprotonated sulfonyl group,[68] it can attract postive metal ions, such as Mn^{2+}, thus confining Mn^{2+} near the cathode and controlling the Mn dissolution. As a result, the PEDOT: PSS coating can imporve the cycling performance of aqueous rechargable Zn-MnO_2 battery.

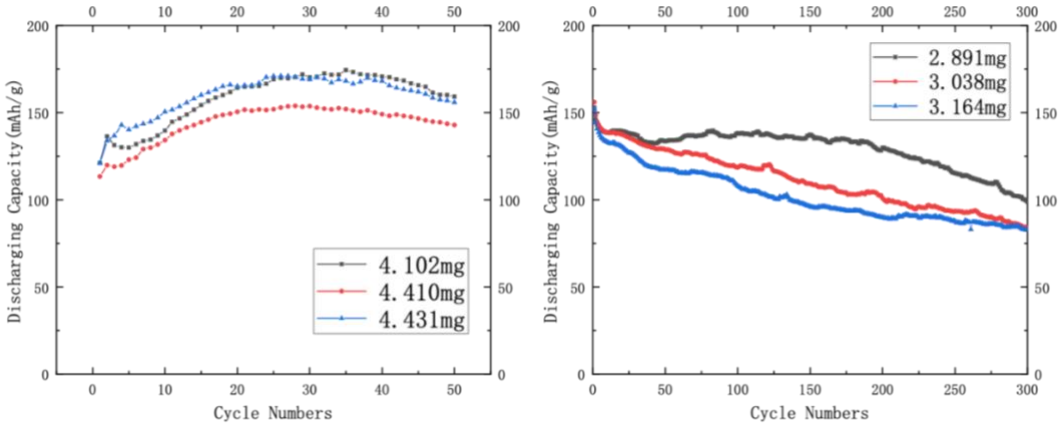

Figure 46 The battery cycling performance of the PEDOT: PSS coated Zn-MnO_2 battery at 50 mA/g (left) and 500 mA/g (right)

The rate performance was also investigated to measure the discharging capacity of the Zn-MnO_2 battery with PEDOT: PSS coating at different discharging current densities and

its reversibility after different current densities. To begin with, the battery was tested at 0.05 A/g for 10 cycles, and then test it for 5 cycles at each discharging rate. As shown in Figure 47, the EM-16 coated battery exhibited a discharging capacity of 270 mAh/g, 210 mAh/g, 125 mAh/g, 50 mAh/g, 25 mAh/g, and 15 mAh/g at 0.05 A/g, 0.1 A/g, 0.2 A/g, 0.5 A/g, 1 A/g, and 2 A/g, respectively. Afterwards, the battery was tested again at 0.05 A/g to see its reversibility, and the batteries with different concentrations of PEDOT: PSS solutions all can reach the similar capacity at 0.05 A/g, which proved the good reversibility for both unmodified and PEDOT: PSS coated cathodes.

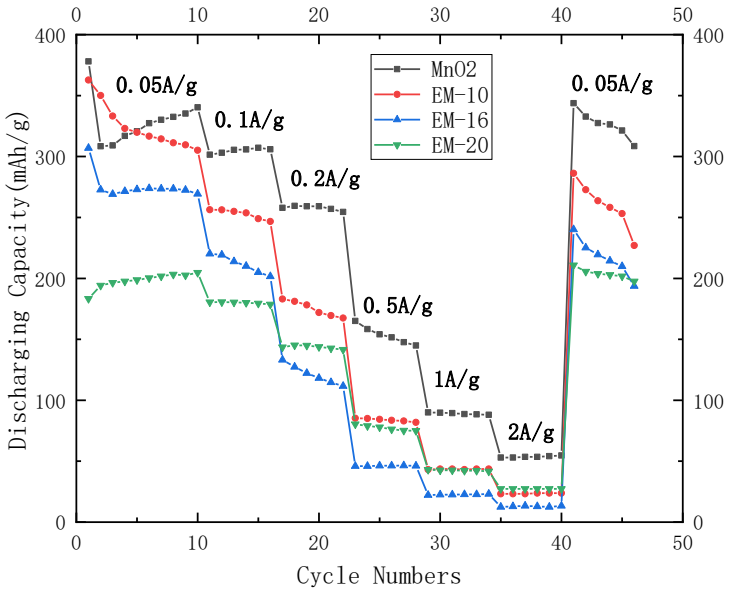

Figure 47 The rate performance of the PEDOT: PSS coated Zn-MnO_2 battery at 0.05 A/g, 0.1 A/g, 0.2 A/g, 0.5 A/g, 1 A/g and 2 A/g

4.5 Conclusions

In conclusion, the PEDOT: PSS solutions with difference concentration have been prepared and successfully coated on top of the ε-MnO_2 cathode by spin coating method.

Moreover, the PEDOT: PSS coated cathode has been characterized using SEM, FTIR, and XPS to explore the morphology and structure of the modified MnO_2 cathode and prove the existence of PEDOT: PSS coating. Zn-MnO_2 batteries with PEDOT: PSS coated cathode have been assembled into coin cells and tested as well. It was found that PEDOT: PSS coating can attract Mn^{2+} through ionic interactions and control the Mn dissolution, resulting in a better battery cycling performance at both 50 mA/g and 500 mA/g.

The PEDOT: PSS has been uniformly coated on the MnO_2 surface observed by SEM. Furthermore, the successful coating of PEDOT: PSS solution on the cathode was demonstrated by FTIR measurements with the identification of standard peaks for C=C bond, S=O bond, C-O bond and S-phenyl bond in FTIR spectra, and by XPS measurements with increased amount of sulfur in the survey and S 2p spectra.

The electrochemical measurements were done to investigate the effect of PEDOT: PSS coating. Though CV test, there was a lager difference between oxidation and reduction peaks, which could be explained by the ionic interactions between the PEDOT: PSS and Zn^{2+} ion. In addition, the battery with PEDOT: PSS coating exhibited a good specific discharging capacity of 270 mAh/g at 50 mA/g, and an excellent cycling performance of 50 cycles with 80% capacity rentention at 50 mA/g and 250 cycles with 80% capacity rentention at 500 mA/g. Besides, the rate capablity was also satisfying since it has a good reversiblity. The improvement in the cycling perfromance could be explain by the ionic interaciton between the sulfonyl group and Mn^{2+}, which can confine most of the Mn^{2+} near the cathode area and improve the cycling performance.

Therefore, the PEDOT: PSS coating on the ε-MnO_2 cathode can improve the cycling performance of the aqueous rechargeable Zn-MnO_2 battery. This easy spin-coating method also gives other researchers a new idea on how to improve the battery cycling performance. The high discharging capacity, high cyclability, high safety, cost effective and environmentally friendly aqueous rechargeable Zn-MnO_2 battery will have more potential usage in the future.

Chapter 5: Summary of the Thesis

Aqueous rechargeable zinc ion battery (ARZIB) has attracted many researchers' attention because of its high energy density, high safety, cost-efficiency and environmental friendliness. MnO_2 is one of the most promising candidates to be applied as cathode in ARZIB system due to its high specific discharge capacity, high safety, high abundance, and low toxicity. However, the electrochemical performance of commercial MnO_2 is not satisfying, and most of researchers are using hydrothermal methods to synthesize MnO_2, which is dangerous and hard to control during the reaction process. Moreover, the Mn dissolution problem impairs the cyclability and the further application of the aqueous rechargeable Zn-MnO_2, and there is a strong and urgent requirement to improve the cycling performance. Therefore, a safe, easy and cost-effective co-precipitation ε-MnO_2 synthesis method was invented, and two effective strategies were proposed and conducted to overcome the Mn dissolution issue by controlling the movement of Mn^{2+} near the cathode through molecule interactions.

The safe, simple, and cost-effective co-precipitation method was used to successfully synthesize the ε-MnO_2 material with a hexagonal unit cells structure of a = 0.280nm, c = 0.445nm. Then the ε-MnO_2 material was made into cathode and assembled into coin cells. The battery showed an excellent discharge capacity of 330 mAh/g at 50 mA/g, a cyclability of 20 cycles with 80% capacity retention, and a good rate capability at different current density between 0.05 A/g and 2.0 A/g.

To improve the cycling performance of the aqueous rechargeable Zn-MnO_2 battery, gelatin solution was applied on top of the MnO_2 cathode through spin coating method. The

gelatin coated battery showed a high discharge capacity of 330 mAh/g at 50 mA/g. More importantly, the cycling performance has been dramatically improved to 1000 cycles with 80% capacity retention at 500 mA/g, which can be explained by the interaction between the gelatin and Mn^{2+}. The gelatin can confine most of the Mn^{2+} near the cathode through hydrogen bonds and van der Waal's force, thus controlling the Mn dissolution problem and improving the cyclability of aqueous rechargeable Zn-MnO_2 batteries.

Another effective strategy is to coat PEDOT: PSS solution on top of the MnO_2 cathode by spin coating method. Since PEDOT: PSS has negatively charged deprotonated sulfonyl group, it could attract metal postive ions through ionic interactions. Therfore, the PEDOT: PSS coating can confine the Mn^{2+} near the cathode and manage the Mn dissolution problem. Consquently, the battery cycling performance has been imporved to 250 cycles at 500 mA/g and 50 cycles at 50 mA/g with both 80% capacity retention.

In conclusion, the ε-MnO_2 material has been successfully synthesized and applied in aqueous rechargeable Zn-MnO_2 battery system with a high discharge capacity of 330 mAh/g. Two effective strategies have been applied to overcome the Mn dissolution problem and improve the battery cyclability up to 1000 cycles with 80% capacity retention without significant influence on the discharging capacity. These research works not only improve the battery cycling performance, but also provide new ideas for other researchers to further enhance the performance of aqueous rechargeable Zn-MnO_2 batteries, and the aqueous rechargeable Zn-MnO_2 battery will have more potential applications in the future.

References

(1) Coyle, E. D.; Simmons, R. A. *Understanding the Global Energy Crisis*; Purdue University Press: West Lafayette, IN, 2014.

(2) Electricity generation mix in advanced economies, 1971-2019. International Energy Angency Wed site. https://www.iea.org/data-and-statistics/charts/electricity-generation-mix-in-advanced-economies-1971-2019 (accessed Apr 16, 2021).

(3) Ibrahim, H.; Ilinca, A.; Perron, J. Energy Storage Systems—Characteristics and Comparisons. *Renew. Sustain. Energy Rev.* **2008**, *12 (5)*, 1221–1250.

(4) Reddy, T.; Linden, D. *Linden's Handbook of Batteries*; McGraw-Hill: Montigny-le-Bretonneux, France, 2010.

(5) Linden, D. *Handbook of Batteries and Fuel Cells*, 7300th ed.; McGraw Hill Higher Education: Maidenhead, England, 1984.

(6) Pillot, C. *The Rechargeable Battery Market and Main Trends 2018 – 2030*; Paris, France, 2019.

(7) *Lead-Acid Batteries for Future Automobiles*; Garche, J., Karden, E., Moseley, P. T., Rand, D. A. J., Eds.; Elsevier Science: London, England, 2017.

(8) *Lead-Acid Battery Technologies: Fundamentals, Materials, and Applications*; Jung, J., Zhang, L., Zhang, J., Eds.; CRC Press: Boca Raton, FL, 2015.

(9) Hannan, M. A.; Hoque, M. M.; Mohamed, A.; Ayob, A. Review of Energy Storage Systems for Electric Vehicle Applications: Issues and Challenges. *Renew. Sustain. Energy Rev.* **2017**, *69*, 771–789.

(10) Babakhani, A.; Rashchi, F.; Zakeri, A.; Vahidi, E. Selective Separation of Nickel and Cadmium from Sulfate Solutions of Spent Nickel–Cadmium Batteries Using Mixtures of D2EHPA and Cyanex 302. *J. Power Sources* **2014**, *247*, 127–133.

(11) Sorahan, T.; Esmen, N. A. Lung Cancer Mortality in UK Nickel-Cadmium Battery Workers, 1947-2000. *Occup. Environ. Med*. **2004**, *61 (2)*, 108–116.

(12) Ren, Z.; Yu, J.; Li, Y.; Zhi, C. Tunable Free-Standing Ultrathin Porous Nickel Film for High Performance Flexible Nickel-Metal Hydride Batteries. *Adv. Energy Mater.* **2018**, *8* (12), 1702467.

(13) Li, M.; Lu, J.; Chen, Z.; Amine, K. 30 Years of Lithium-Ion Batteries. *Adv. Mater.* **2018**, *30* (33), e1800561.

(14) Kraytsberg, A.; Ein-Eli, Y. Higher, Stronger, Better… A Review of 5 Volt Cathode Materials for Advanced Lithium-Ion Batteries. *Adv. Energy Mater.* **2012**, *2* (8), 922–939.

(15) *Electrolytes for Lithium and Lithium-Ion Batteries*; Jow, R. T., Xu, K., Borodin, O., Ue, M., Eds.; Springer: New York, NY, 2014.

(16) Warner, J. T. *The Handbook of Lithium-Ion Battery Pack Design: Chemistry, Components, Types and Terminology*; Elsevier Science Publishing: Philadelphia, PA, 2015.

(17) Liao, H.; Zhang, H.; Qin, G.; Hong, H.; Li, Z.; Lin, Y.; Li, L. Novel Core-Shell PS-Co -PBA@SiO_2 Nanoparticles Coated on PP Separator as "Thermal Shutdown Switch" for High Safety Lithium-Ion Batteries. *Macromol. Mater. Eng.* **2017**, *302* (11), 1700241.

(18) *Behaviour of Lithium-Ion Batteries in Electric Vehicles: Battery Health, Performance, Safety, and Cost*, 1st ed.; Pistoia, G., Liaw, B., Eds.; Springer International Publishing: Cham, Switzerland, 2018.

(19) Song, J.; Xu, K.; Liu, N.; Reed, D.; Li, X. Crossroads in the Renaissance of Rechargeable Aqueous Zinc Batteries. *Mater. Today (Kidlington)* **2021**.

https://doi.org/10.1016/j.mattod.2020.12.003

(20) Aurbach, D. Understanding Batteries. *Electrochim. Acta* **2002**, *47* (21), 3561

(21) Oh, S.; Kim, S. Aqueous zinc sulfate (II) rechargeable cell containing manganese (II) salt and carbon powder. US 6187475 B1, February 13, 2001.

(22) Song, M.; Tan, H.; Chao, D.; Fan, H. J. Recent Advances in Zn-Ion Batteries. *Adv. Funct. Mater.* **2018**, *28* (41), 1802564.

(23) Pan, H.; Shao, Y.; Yan, P.; Cheng, Y.; Han, K. S.; Nie, Z.; Wang, C.; Yang, J.; Li, X.; Bhattacharya, P.; Mueller, K. T.; Liu, J. Reversible Aqueous Zinc/Manganese Oxide Energy Storage from Conversion Reactions. *Nat. Energy* **2016**, *1* (5), 16039.

(24) Selvakumaran, D.; Pan, A.; Liang, S.; Cao, G. A Review on Recent Developments and Challenges of Cathode Materials for Rechargeable Aqueous Zn-Ion Batteries. *J. Mater. Chem. A.* **2019**, *7* (31), 18209–18236.

(25) Xu, C.; Li, B.; Du, H.; Kang, F. Energetic Zinc Ion Chemistry: The Rechargeable Zinc Ion Battery. *Angew. Chem. Int. Ed Engl.* **2012**, *51* (4), 933–935.

(26) Yaroshevsky, A. A. Abundances of Chemical Elements in the Earth's Crust. *Geochem. Int.* **2006**, *44* (1), 48–55.

(27) Liu, Y.; Shi, Q.; Wu, Y.; Wang, Q.; Huang, J.; Chen, P. Highly Efficient Dendrite Suppressor and Corrosion Inhibitor Based on Gelatin/Mn^{2+} Co-Additives for Aqueous Rechargeable Zinc-Manganese Dioxide Battery. *Chem. Eng. J.* **2021**, *407* (127189), 127189.

(28) Chen, L.; An, Q.; Mai, L. Recent Advances and Prospects of Cathode Materials for Rechargeable Aqueous Zinc-Ion Batteries. *Adv. Mater. Interfaces* **2019**, *6* (17), 1900387.

(29) Nie, P.; Shen, L.; Luo, H.; Ding, B.; Xu, G.; Wang, J.; Zhang, X. Prussian Blue Analogues: A New Class of Anode Materials for Lithium Ion Batteries. *J. Mater. Chem. A.* **2014**, *2* (16), 5852–5857.

(30) Kundu, D.; Oberholzer, P.; Glaros, C.; Bouzid, A.; Tervoort, E.; Pasquarello, A.; Niederberger, M. Organic Cathode for Aqueous Zn-Ion Batteries: Taming a Unique Phase Evolution toward Stable Electrochemical Cycling. *Chem. Mater.* **2018**, *30* (11), 3874–3881.

(31) Liu, Y.; Zhi, J.; Sedighi, M.; Han, M.; Shi, Q.; Wu, Y.; Chen, P. Mn^{2+} Ions Confined

by Electrode Microskin for Aqueous Battery beyond Intercalation Capacity. *Adv. Energy Mater.* **2020**, *10* (42), 2002578.

(32) Lee, B.; Lee, H. R.; Kim, H.; Chung, K. Y.; Cho, B. W.; Oh, S. H. Elucidating the Intercalation Mechanism of Zinc Ions into α-MnO_2 for Rechargeable Zinc Batteries. *Chem. Commun. (Camb.)* **2015**, *51* (45), 9265–9268.

(33) Sun, W.; Wang, F.; Hou, S.; Yang, C.; Fan, X.; Ma, Z.; Gao, T.; Han, F.; Hu, R.; Zhu, M.; Wang, C. Zn/MnO_2 Battery Chemistry with H^+ and Zn^{2+} Coinsertion. *J. Am. Chem. Soc.* **2017**, *139* (29), 9775–9778..

(34) Huang, Y.; Mou, J.; Liu, W.; Wang, X.; Dong, L.; Kang, F.; Xu, C. Novel Insights into Energy Storage Mechanism of Aqueous Rechargeable Zn/MnO_2 Batteries with Participation of Mn^{2+}. *Nano-Micro Lett.* **2019**, *11* (1).

(35) Chao, D.; Zhou, W.; Ye, C.; Zhang, Q.; Chen, Y.; Gu, L.; Davey, K.; Qiao, S. An Electrolytic Zn–MnO_2 Battery for High-Voltage and Scalable Energy Storage. *Angew. Chemie Int. Ed Engl.* **2019**, *58* (23), 7823–7828.

(36) Wang, A.; Zhou, W.; Huang, A.; Chen, M.; Chen, J.; Tian, Q.; Xu, J. Modifying the Zn Anode with Carbon Black Coating and Nanofibrillated Cellulose Binder: A Strategy to Realize Dendrite-Free Zn-MnO2 Batteries. *J. Colloid Interface Sci.* **2020**, *577*, 256–264.

(37) Liu, X.; Yi, J.; Wu, K.; Jiang, Y.; Liu, Y.; Zhao, B.; Li, W.; Zhang, J. Rechargeable Zn-MnO_2 Batteries: Advances, Challenges and Perspectives. *Nanotechnology* **2020**, *31* (12), 122001.

(38) Kim, S. J.; Wu, D.; Sadique, N.; Quilty, C. D.; Wu, L.; Marschilok, A. C.; Takeuchi, K. J.; Takeuchi, E. S.; Zhu, Y. Unraveling the Dissolution-Mediated Reaction Mechanism of α-MnO_2 Cathodes for Aqueous Zn-Ion Batteries. *Small* **2020**, *16* (48), 2005406.

(39) Zeng, X.; Liu, J.; Mao, J.; Hao, J.; Wang, Z.; Zhou, S.; Ling, C. D.; Guo, Z. Toward a Reversible Mn^{4+}/Mn^{2+} Redox Reaction and Dendrite-Free Zn Anode in Near-

Neutral Aqueous Zn/MnO_2 Batteries via Salt Anion Chemistry. *Adv. Energy Mater.* **2020**, *10* (32), 1904163.

(40) Chen, M.; Chen, J.; Zhou, W.; Han, X.; Yao, Y.; Wong, C. Realizing an All-Round Hydrogel Electrolyte toward Environmentally Adaptive Dendrite-Free Aqueous Zn–MnO_2 Batteries. *Adv. Mater.* **2021**, *33* (9), 2007559.

(41) Tang, B.; Shan, L.; Liang, S.; Zhou, J. Issues and Opportunities Facing Aqueous Zinc-Ion Batteries. *Energy Environ. Sci.* **2019**, *12* (11), 3288–3304.

(42) Yang, J.; Cao, J.; Peng, Y.; Yang, W.; Barg, S.; Liu, Z.; Kinloch, I. A.; Bissett, M. A.; Dryfe, R. A. W. Unravelling the Mechanism of Rechargeable Aqueous Zn–MnO_2 Batteries: Implementation of Charging Process by Electrodeposition of MnO_2. *ChemSusChem* **2020**, *13* (16), 4103–4110.

(43) He, P.; Chen, Q.; Yan, M.; Xu, X.; Zhou, L.; Mai, L.; Nan, C.-W. Building Better Zinc-Ion Batteries: A Materials Perspective. *EnergyChem* **2019**, *1* (3), 100022.

(44) Higashi, S.; Lee, S. W.; Lee, J. S.; Takechi, K.; Cui, Y. Avoiding Short Circuits from Zinc Metal Dendrites in Anode by Backside-Plating Configuration. *Nat. Commun.* **2016**, *7* (1), 11801.

(45) Lu, W.; Xie, C.; Zhang, H.; Li, X. Inhibition of Zinc Dendrite Growth in Zinc-Based Batteries. *ChemSusChem* **2018**, *11* (23), 3996–4006.

(46) Fang, G.; Zhu, C.; Chen, M.; Zhou, J.; Tang, B.; Cao, X.; Zheng, X.; Pan, A.; Liang, S. Suppressing Manganese Dissolution in Potassium Manganate with Rich Oxygen Defects Engaged High-Energy-Density and Durable Aqueous Zinc-Ion Battery. *Adv. Funct. Mater.* **2019**, *29* (15), 1808375.

(47) Wu, B.; Zhang, G.; Yan, M.; Xiong, T.; He, P.; He, L.; Xu, X.; Mai, L. Graphene Scroll-Coated α-MnO_2 Nanowires as High-Performance Cathode Materials for Aqueous Zn-Ion Battery. *Small* **2018**, *14* (13), 1703850.

(48) Chamoun, M.; Brant, W. R.; Tai, C. W.; Karlsson, G.; Noréus, D. Rechargeability of Aqueous Sulfate Zn/MnO2 Batteries Enhanced by Accessible Mn^{2+} Ions. *Energy*

Storage Mater. **2018**, *15*, 351–360.

(49) Zhao, K.; Wang, C.; Yu, Y.; Yan, M.; Wei, Q.; He, P.; Dong, Y.; Zhang, Z.; Wang, X.; Mai, L. Ultrathin Surface Coating Enables Stabilized Zinc Metal Anode. *Adv. Mater. Interfaces* **2018**, *5* (16), 1800848.

(50) Qiu, W.; Li, Y.; You, A.; Zhang, Z.; Li, G.; Lu, X.; Tong, Y. High-Performance Flexible Quasi-Solid-State Zn-MnO_2 Battery Based on MnO_2 Nanorod Arrays Coated 3D Porous Nitrogen-Doped Carbon Cloth. *J. Mater. Chem. A* **2017**, *5* (28), 14838–14846.

(51) Kang, Z.; Wu, C.; Dong, L.; Liu, W.; Mou, J.; Zhang, J.; Chang, Z.; Jiang, B.; Wang, G.; Kang, F.; Xu, C. 3D Porous Copper Skeleton Supported Zinc Anode toward High Capacity and Long Cycle Life Zinc Ion Batteries. *ACS Sustain. Chem. Eng.* **2019**, *7* (3), 3364–3371.

(52) Djagny, K. B.; Wang, Z.; Xu, S. Gelatin: A Valuable Protein for Food and Pharmaceutical Industries: Review. *Crit. Rev. Food Sci. Nutr.* **2001**, *41* (6), 481–492.

(53) Gelatin https://chembam.com/resources-for-students/the-chemistry-of/gelatin/ (accessed Apr 16, 2021).

(54) Kommareddy, S.; Shenoy, D. B.; Amiji, M. M. Gelatin Nanoparticles and Their Biofunctionalization. *Nanotechnologies for the Life Sciences*; Wiley-VCH Verlag GmbH & Co. KGaA: Weinheim, Germany, 2007.

(55) COURTS, A. The N-Terminal Amino Acid Residues of Gelatin. 2. Thermal Degradation. *Biochem. J.* **1954**, *58* (1), 74–79.

(56) Farrugia, C. A.; Groves, M. J. Gelatin Behaviour in Dilute Aqueous Solution: Designing a Nanoparticulate Formulation. *J. Pharm. Pharmacol.* **1999**, *51* (6), 643–649.

(57) Idson, B.; Braswell, E. Gelatin. In *Advances in Food Research Volume 7*; Elsevier, 1957; pp 235–338.

(58) Bender, A. E.; Miller, D. S.; Tunnah, E. J. The Biological Value of Gelatin. *Chem. Ind* **1953**, No. 30.

(59) Karim, A. A.; Bhat, R. Fish Gelatin: Properties, Challenges, and Prospects as an Alternative to Mammalian Gelatins. *Food Hydrocoll.* **2009**, *23* (3), 563–576

(60) Cho, S. M.; Kwak, K. S.; Park, D. C.; Gu, Y. S.; Ji, C. I.; Jang, D. H.; Lee, Y. B.; Kim, S. B. Processing Optimization and Functional Properties of Gelatin from Shark (Isurus Oxyrinchus) Cartilage. *Food Hydrocoll.* **2004**, *18* (4), 573–579.

(61) Liu, H. Y.; Li, D.; Guo, S. D. Extraction and Properties of Gelatin from Channel Catfish (Ietalurus Punetaus) Skin. *Lebenson. Wiss. Technol.* **2008**, *41* (3), 414–419.

(62) Gómez-Guillén, M. C.; Ihl, M.; Bifani, V.; Silva, A.; Montero, P. Edible Films Made from Tuna-Fish Gelatin with Antioxidant Extracts of Two Different Murta Ecotypes Leaves (Ugni Molinae Turcz). *Food Hydrocoll.* **2007**, *21* (7), 1133–1143

(63) Avena-Bustillos, R. J.; Olsen, C. W.; Olson, D. A.; Chiou, B.; Yee, E.; Bechtel, P. J.; McHugh, T. H. Water Vapor Permeability of Mammalian and Fish Gelatin Films. *J. Food Sci.* **2006**, *71* (4), E202–E207.

(64) Li, H.; Han, C.; Huang, Y.; Huang, Y.; Zhu, M.; Pei, Z.; Xue, Q.; Wang, Z.; Liu, Z.; Tang, Z.; Wang, Y.; Kang, F.; Li, B.; Zhi, C. An Extremely Safe and Wearable Solid-State Zinc Ion Battery Based on a Hierarchical Structured Polymer Electrolyte. *Energy Environ. Sci.* **2018**, *11* (4), 941–951.

(65) Wu, W. Effect of Gelatin Additive on Microstructure and Composition of Electrodeposited Rhenium–Nickel Alloys in Aqueous Solutions. *Appl. Phys. A Mater. Sci. Process.* **2016**, *122* (12).

(66) *Science and Technology of Gelatin*; Ward, A. G., Courts, A., Eds.; Academic Press: San Diego, CA, 1977.

(67) Han, Q.; Chi, X.; Liu, Y.; Wang, L.; Du, Y.; Ren, Y.; Liu, Y. An Inorganic Salt Reinforced Zn^{2+}-Conducting Solid-State Electrolyte for Ultra-Stable Zn Metal Batteries. *J. Mater. Chem. A.* **2019**, *7* (39), 22287–22295.

(68) Ko, I. H.; Kim, S. J.; Lim, J.; Yu, S. H.; Ahn, J.; Lee, J. K.; Sung, Y. E. Effect of PEDOT:PSS Coating on Manganese Oxide Nanowires for Lithium Ion Battery Anodes. *Electrochim. Acta* **2016**, *187*, 340–347.

(69) Sun, K.; Zhang, S.; Li, P.; Xia, Y.; Zhang, X.; Du, D.; Isikgor, F. H.; Ouyang, J. Review on Application of PEDOTs and PEDOT:PSS in Energy Conversion and Storage Devices. *J. Mater. Sci. Mater. Electron.* **2015**, *26* (7), 4438–4462.

(70) What is Denatron? https://advancedcoatings.nagasechemtex.co.jp/en/about/ (accessed Apr 16, 2021).

(71) Groenendaal, L.; Jonas, F.; Freitag, D.; Pielartzik, H.; Reynolds, J. R. Poly(3,4-Ethylenedioxythiophene) and Its Derivatives: Past, Present, and Future. *Adv. Mater.* **2000**, *12* (7), 481–494.

(72) Rattan, S.; Singhal, P.; Verma, A. L. Synthesis of PEDOT:PSS (Poly(3,4-Ethylenedioxythiophene))/Poly(4-Styrene Sulfonate))/ Ngps (Nanographitic Platelets) Nanocomposites as Chemiresistive Sensors for Detection of Nitroaromatics. *Polym. Eng. Sci.* **2013**, *53* (10), 2045–2052.

(73) Thomas, J. P.; Zhao, L.; McGillivray, D.; Leung, K. T. High-Efficiency Hybrid Solar Cells by Nanostructural Modification in PEDOT:PSS with Co-Solvent Addition. *J. Mater. Chem. A* **2014**, *2* (7), 2383–2389.

(74) Thomas, J. P.; Shi, Q.; Abd-Ellah, M.; Zhang, L.; Heinig, N. F.; Leung, K. T. Charge Transfer in Nanowire-Embedded PEDOT:PSS and Planar Heterojunction Solar Cells. *ACS Appl. Mater. Interfaces* **2020**, *12* (10), 11459–11466.

(75) Zeng, Y.; Zhang, X.; Meng, Y.; Yu, M.; Yi, J.; Wu, Y.; Lu, X.; Tong, Y. Achieving Ultrahigh Energy Density and Long Durability in a Flexible Rechargeable Quasi-Solid-State Zn–MnO2 Battery. *Adv. Mater.* **2017**, *29* (26), 1–7.

(76) Scanning Electron Microscopy - Nanoscience Instruments.

https://www.nanoscience.com/techniques/scanning-electron-microscopy/ (accessed Apr 16, 2021)

(77) Ni, C. Scanning Electron Microscopy (SEM). In *Encyclopedia of Tribology*; Springer US: Boston, MA, 2013; pp 2977–2982.

(78) Rochow, T. G.; Rochow, E. G. Scanning Electron Microscopy. In *An Introduction to Microscopy by Means of Light, Electrons, X-Rays, or Ultrasound*; Springer US: Boston, MA, 1978; pp 273–298.

(79) Unruh, D. K.; Forbes, T. Z. X-Ray Diffraction Techniques. In *Analytical Geomicrobiology*; Cambridge University Press, 2019; pp 215–237.

(80) Stanjek, H.; Häusler, W. Basics of X-Ray Diffraction. *Hyperfine Interact.* **2004**, *154* (1–4), 107–119.

(81) X-ray Powder Diffraction (XRD).

https://serc.carleton.edu/research_education/geochemsheets/techniques/XRD.html (accessed Apr 16, 2021)

(82) Holzwarth, U.; Gibson, N. The Scherrer Equation versus the "Debye-Scherrer Equation." *Nat. Nanotechnol.* **2011**, *6* (9), 534–534.

(83) Fourier Transform Infrared Spectroscopy - an overview | ScienceDirect Topics https://www-sciencedirect-com.proxy.lib.uwaterloo.ca/topics/engineering/fourier-transform-infrared-spectroscopy (accessed Apr 16, 2021).

(84) Fourier Transform Infrared Spectroscopy (FTIR) - Chemistry LibreTexts https://chem.libretexts.org/Courses/Howard_University/Howard%3A_Physical_Chemistry_Laboratory/14._Fourier_Transform_Infrared_Spectroscopy_(FTIR) (accessed Apr 16, 2021).

(85) X-Ray Photoelectron Spectroscopy - an overview | ScienceDirect Topics https://www-sciencedirect-com.proxy.lib.uwaterloo.ca/topics/chemistry/x-ray-photoelectron-spectroscopy (accessed Apr 16, 2021).

(86) X-ray photoelectron spectroscopy - Wikipedia.

https://en.wikipedia.org/wiki/X-ray_photoelectron_spectroscopy (accessed Apr 16,

2021)

(87) Thermo Scientific XPS: What is XPS.

https://xpssimplified.com/whatisxps-photoemission.php (accessed Apr 16, 2021).

(88) Elgrishi, N.; Rountree, K. J.; McCarthy, B. D.; Rountree, E. S.; Eisenhart, T. T.; Dempsey, J. L. A Practical Beginner's Guide to Cyclic Voltammetry. *J. Chem. Educ.* **2018**, *95* (2), 197–206.

(89) Guy, O. J.; Walker, K. A. D. Graphene Functionalization for Biosensor Applications. In *Silicon Carbide Biotechnology*; Elsevier, 2016; pp 85–141.

(90) Cyclic voltammetry - Wikipedia

https://en.wikipedia.org/wiki/Cyclic_voltammetry (accessed Apr 16, 2021).

(91) Cyclic Voltammogram - YouTube

https://www.youtube.com/watch?v=1f92vGOridg (accessed Apr 16, 2021).

(92) BTS4000 triple output range testers – Neware battery testers

https://newarebattery.com/neware-bts4000-series-customizable-output-power-range-and-functions/bts4000-triple-output-range-testers/ (accessed Apr 16, 2021).

(93) Shi, Q.; Liu, Y. and Chen, P. Preparation Method and Application of Manganese Dioxide Electrode. CN110563045A, December 13, **2019**.

(94) Lee, C. Y.; Chuang, S. M.; Lee, S. J.; Hung, I. M.; Hsieh, C. Te; Chang, Y. M.; Huang, Y. P. Flexible Micro Sensor for In-Situ Monitoring Temperature and Voltage of Coin Cells. *Sensors Actuators, A Phys.* **2015**, *232*, 214–222.

(95) Compact Hydraulic Crimping Machine: One for All Button Cells of CR2016 , CR2025 & CR2032 and CR2325 by Optional Die- EQ-MSK-110

https://www.mtixtl.com/CompactHydraulicCrimpingMachineOneforAllButtonCells-MSK-110.aspx (accessed Apr 16, 2021).

(96) Chemat precision spin-coater AC/DC input 115 V AC| Sigma-Aldrich

https://www.sigmaaldrich.com/catalog/product/aldrich/z551562?lang=en&region=CA (accessed Apr 16, 2021).

(97) Kim, C. H.; Akase, Z.; Zhang, L.; Heuer, A. H.; Newman, A. E.; Hughes, P. J. The Structure and Ordering of ε-MnO_2. *J. Solid State Chem.* **2006**, *179* (3), 753–774.

(98) Feng, Z.; Chen, X.; Qiao, L.; Lipson, A. L.; Fister, T. T.; Zeng, L.; Kim, C.; Yi, T.; Sa, N.; Proffit, D. L.; Burrell, A. K.; Cabana, J.; Ingram, B. J.; Biegalski, M. D.; Bedzyk, M. J.; Fenter, P. Phase-Controlled Electrochemical Activity of Epitaxial Mg-Spinel Thin Films. *ACS Appl. Mater. Interfaces* **2015**, *7* (51), 28438–28443.

(99) Ederer, J.; Janoš, P.; Ecorchard, P.; Tolasz, J.; Štengl, V.; Beneš, H.; Perchacz, M.; Pop-Georgievski, O. Determination of Amino Groups on Functionalized Graphene Oxide for Polyurethane Nanomaterials: XPS Quantitation vs. Functional Speciation. *RSC Adv.* **2017**, *7* (21), 12464–12473.

(100) Guena, T.; Leblanc, P. How Depth of Discharge Affects the Cycle Life of Lithium-Metal-Polymer Batteries. In *INTELEC, International Telecommunications Energy Conference (Proceedings)*; **2006**. https://doi.org/10.1109/INTLEC.2006.251641.

(101) IR Spectrum Table & Chart | Sigma-Aldrich

https://www.sigmaaldrich.com/technical-documents/articles/biology/ir-spectrum-table.html (accessed Apr 16, 2021).

(102) Yemata, T. A.; Zheng, Y.; Kyaw, A. K. K.; Wang, X.; Song, J.; Chin, W. S.; Xu, J. Modulation of the Doping Level of PEDOT:PSS Film by Treatment with Hydrazine to Improve the Seebeck Coefficient. *RSC Adv.* **2020**, *10* (3), 1786–1792.

(103) Tai, G.; Zeng, T.; Yu, J.; Zhou, J.; You, Y.; Wang, X.; Wu, H.; Sun, X.; Hu, T.; Guo, W. Fast and Large-Area Growth of Uniform MoS2 Monolayers on Molybdenum Foils. *Nanoscale* **2016**, *8* (4), 2234–2241.

(104) Crispin, X.; Marciniak, S.; Osikowicz, W.; Zotti, G.; van der Gon, A. W. D.; Louwet, F.; Fahlman, M.; Groenendaal, L.; De Schryver, F.; Salaneck, W. R. Conductivity, Morphology, Interfacial Chemistry, and Stability of Poly(3,4-Ethylene

Dioxythiophene)-Poly(Styrene Sulfonate): A Photoelectron Spectroscopy Study. *J. Polym. Sci. Part B Polym. Phys.* **2003**, *41* (21), 2561–2583.

(105) Kim, Y. H.; Sachse, C.; Machala, M. L.; May, C.; Müller-Meskamp, L.; Leo, K. Highly Conductive PEDOT:PSS Electrode with Optimized Solvent and Thermal Post-Treatment for ITO-Free Organic Solar Cells. *Adv. Funct. Mater.* **2011**, *21* (6), 1076–1081.